Polarity and Timing of the Deformation along the Jinsha Suture Zone (Yushu area, Northeastern Tibet)

Goussin, Fanny[1]; Guillot, Stéphane[1] ; Ruffet Gilles[2]; Poujol, Marc[2]; Oliot, Émilien[3]; Replumaz, Anne[1]; Cordier Carole[1]; Dupont-Nivet Guillaume[2,4]; Roperch Pierrick[2]

[1] Univ. Grenoble Alpes, Univ. Savoie Mont Blanc, Univ. Gustave Eiffel, CNRS, IRD, ISTerre, 38000 Grenoble, France

[2] CNRS, Université de Rennes, UMR 6118 Géosciences Rennes, 35042 Rennes Cedex, France

[3] UMR 5243 Géosciences Montpellier, CNRS, Université de Montpellier, 34095, Montpellier Cedex 05, France

[4] Institut für Erd- und Umweltwissenschaften, Universität Potsdam, Potsdam, Germany

Keypoints

- The Jinsha Suture in the Yushu area (NE Tibet) recorded three main tectono-metamorphic events.
- Deformed samples yield Early Triassic to Middle Jurassic ages, related to the closure of the Songpan-Ganze basin of the Paleo-Tethys.
- The Jinsha suture was not reactivated at >200°C during Cenozoic post-collisional regional shortening.

Abstract

The Tibetan Plateau was formed by intense Cenozoic shortening (up to 1100 km) of a composite "proto-Tibet", itself the product of a long Paleozoic and Mesozoic history of accretion of Gondwana-derived continental fragments and volcanic arcs against the Asian continental margin. The difficult access and the scarcity of outcrops have long limited the possibilities of studying these Mesozoic suture zones in the heart of the Plateau. In this work, we present new U-Pb and $^{40}Ar/^{39}Ar$ ages from the highly deformed units of the Yushu mélange, along the Jinsha Suture in the northeastern Qiangtang terrane. Early Triassic (c. 253 Ma) to Middle Jurassic ages (c. 165 Ma) complement the existing dataset and help to refine the chronology of the Paleo-Tethyan oceanic subductions which have structured the northeastern part of the Qiangtang terrane. The Yushu mélange records at least three successive tectono-magmatic events. The opening of a back-arc basin during the northward

Paleo-Tethyan subduction along the Longmu Co-Shuanghu Suture during Early to Middle Triassic; then its closure during the southward subduction of the Songpan-Ganze Ocean along the Jinsha Suture in Late Triassic. Finally, a shortening phase related to the continental collision of the Songpan-Ganze and Qiangtang blocks from Late Triassic to Early-Middle Jurassic. No evidence for any high- or mid-temperature Cenozoic reactivation of the Jinsha suture in our study area is recorded.

1. Introduction

"Pre-collisional" tectonics of Tibet, defined as the tectonics preceding the collision of India with Asia in the early Cenozoic, are increasingly regarded as a major component of the buildup of the present Tibetan plateau (Murphy et al., 1997; Kapp and DeCelles, 2019). From the Paleozoic to the Mesozoic, the continental terranes composing Tibet, i.e. the North-Qiangtang, South-Qiangtang, and Lhasa terranes (Figure 1a), together with other micro-continents such as the Tarim, Qaidam, North and South China, Yidun, Sibumasu and Indochina blocks, drifted from Gondwana and were accreted together to form the southern margin of Asia (B. Huang et al., 2018). The oceanic basins (Proto-Tethys, Paleo-Tethys and Meso-Tethys) separating the main blocks were progressively subducted (Figure 1b). Each of these subductions and suture accretions represented major tectonic events at the Asian scale (Jolivet, 2017; Metcalfe, 2021). Among them, the closure of the Paleo-Tethys ocean, which resulted in the amalgamation of the Qiangtang terranes and the formation of the huge Songpan-Ganze accretionary wedge, has received much attention in the past two decades highlighting various reactivations (e.g. Kapp et al., 2000, 2003; Pullen et al., 2008; Roger et al., 2000, 2003, 2008)

The Western Jinsha and the Ganze-Litang sutures are the boundary between the North Qiangtang and Songpan-Ganze terranes that constitute the present-day Central and North Tibetan Plateau (Figure 1a). In the recent years, several studies have focused on acquiring precise ages and geochemical data on the pre-Cenozoic magmatic rocks that line the Western Jinsha suture between the North Qiangtang and Songpan-Ganze terranes (Chen et al., 2005; Gu et al., 2013; Jin, 2006; G.-M. Li et al., 2015; J. Li et al., 2012; B. Liu, Ma, Guo, Sun, et al., 2016; B. Liu, Ma, Guo, Xiong, et al., 2016; Yan Liu et al., 2019; Yin Liu et al., 2010, 2014, 2019, 2021; Tan et al., 2020; B. Z. Wang et al., 2008; Yang et al., 2012; Yong et al., 2011; H. Zhang et al., 2017; Zhao, Fu, et al., 2015; Zhao, Tan, et al., 2015). These studies have revealed that magmatism spans from the Carboniferous to the Early Jurassic (Yin Liu et al., 2021), but neither the spatio-temporal repartition of these rocks, nor their mixed geochemical affinities (arc, but also OIB, high-Mg rocks, adakite-like signatures,...) have yet truly resolved the ambiguity about the number of Paleo-Tethyan subductions as well as their polarities (see section 2.1).

By comparison, styles and ages of the deformation events across the Western Jinsha suture are much less documented, with only three ages obtained on deformed rocks, from c. 244 Ma (U-Pb on monazite) to c. 195 Ma ($^{40}Ar/^{39}Ar$ on muscovite; Roger et al., 2003; Yang et al., 2012). Yet, dating and characterizing deformation events across this key Paleo-Tethyan

tectonic structure would give complementary information that may help to better constrain the existing geodynamic models.

In this study, we conducted a structural field work and $^{40}Ar/^{39}Ar$ and zircon U-Pb geochronological analyses of deformed rocks from the Jinsha suture zone in the Yushu area (northeastern Qiangtang, Figure 2b). Our results complement the study of Yang et al., (2012), and provide new insights into the protracted and polyphased history of the northern Qiangtang margin, from the Late Paleozoic to the Mesozoic.

history of the northern Qiangtang margin, from the Late Paleozoic to the Mesozoic.

2. Regional Geological Setting

2.1 Closure of the Paleo-Tethys from the Paleozoic to the Mesozoic

The geodynamic evolution of the Paleo-Tethys has long been subject to discussion, and fundamental questions such as the number, shapes and sizes of the Paleo-Tethyan oceanic realms, as well as the polarity of subduction zones, are still debated (Kapp et al., 2000; Yin Liu et al., 2021; Pullen et al., 2008, 2011; Reid et al., 2005, 2007; Roger et al., 2010; Yang et al., 2012, 2014; Yin & Harrison, 2000).

Most authors propose that the Songpan-Ganze terrane represents a former main oceanic domain of the Paleo-Tethys, the Songpan-Ganze Ocean, that separated the Qaidam and North China blocks from the Qiangtang and South China blocks during Paleozoic times (Figure 1b). Northward subduction of the northern edge of this basin is attested by the Kunlun-Anyemaqen suture which comprises ophiolitic assemblages (Konstantinovskaia et al., 2003) and volcanic arc magmatism in the Kunlun dated from 260 to 200 Ma (Harris et al., 1988; Roger et al., 2003, 2008). This subduction led to the complete closure of the northeastern branch of the basin, followed by continental subduction of the South China margin below the North China craton, which resulted in the Qinlin-Dabie Ultra High Pressure belt (Hacker et al., 1998; S. Li et al., 2007; Rowley et al., 1997).

To the south, there is now a consensus that the Songpan-Ganze Ocean subducted southward beneath the Qiangtang and Yidun terranes along the Western Jinsha and Ganze-Litang sutures, at least from the Middle to Late Triassic (Yang et al., 2014; Figure 1b), producing the Yushu and Zhiduo arcs in Northern Qiangtang (c. 217-205 Ma; Roger et al., 2003; Yang et al., 2012), and the eastern Yidun arc (c. 219-216 Ma; Reid et al., 2007). During this final

closure, the large deposits of detrital sediments filling the Songpan-Ganze Ocean were intensely folded and faulted, resulting in a huge accretionary fold-and-thrust belt.

The early evolution of the North Qiangtang margin is more discussed. In particular, the former existence of a second Paleo-Tethyan oceanic basin, separating the North Qiangtang terrane from the South Qiangtang terrane until the Middle or Late Triassic, is still highly debated. This hypothesis is supported by the presence, in the center of the Qiangtang terrane, of the oldest ophiolitic rocks on the Tibetan Plateau (437-501 Ma; Zhai et al., 2016), and of Triassic high-pressure rocks, which define the Longmu Co-Shuangu suture. However, the eastward continuity of this suture is hard to delineate. Kapp et al. (2000, 2003) consider that the Central Qiangtang high pressure rocks (also named Central Qiangtang Metamorphic Belt, CQMB; Figure 1b) represent an exhumed metamorphic dome rather than an *in situ* suture zone. Conversely, recent paleomagnetic data tend to support the presence of a large ocean between the North and South Qiangtang, at least during the Permian: they reveal that the North Qiangtang terrane rifted away from Gondwana prior to the Permian (Song et al., 2017) and was near the equator by late Permian times (Ma et al., 2019), whereas the Permian strata in the South Qiangtang terrane presents evidences of higher latitudes at that time, such as glacio-marine deposits and cold-water fauna (Shangyou et al., 1990; X. Wang et al., 2021).

In the Northern Qiangtang terrane, and especially in an area from Zhiduo in the NW to Litang in the SE, encompassing the Yushu region, widespread Late Permian to Late Triassic magmatic and volcanodetritic rocks have been used to discuss the early Paleo-Tethyan geodynamics (Figure 2a). Some authors propose that the oldest, Permo-Triassic rocks which form the Zhaduo arc in Northern Qiangtang (c. 275-248 Ma; Yang et al., 2011), and the Jomda-Weixi arc in the Litang region (c. 272-229 Ma; Reid et al., 2005, 2007; Yang et al., 2014) result from a northward subduction along the Longmu Co-Shuangu suture beneath the North Qiangtang terrane. From the Yushu to Litang regions, rocks older than 227 Ma are indeed affected by an early phase of deformation characterized by top-N asymmetrical, steeply plunging fabrics, which may relate to this subduction event (Yang et al., 2014). Metamorphic rocks from the central Qiangtang terrane indicate peak eclogitic conditions at c. 244-230 Ma (Dan et al., 2018; Pullen et al., 2008) and exhumation at c. 214-207 Ma (Dan et al., 2018; Kapp et al., 2003; Q.-G. Zhai et al., 2011), that can be ascribed to this subduction.

Other authors consider that only southward subductions occurred along the Northern Qiangtang and Yidun margin, accounting for all the Late Permian to Late Triassic magmatism (Yin Liu et al., 2021; Pullen et al., 2008). Based on the apparent migration pattern of magmatic rocks in the Zhiduo and Yushu regions, Liu et al. (2021) propose three magmatic phases: the first one, south-younging from 312 to 252 Ma would correspond to a subduction advance due to a resisting slab; the second, from 249 to 237 Ma, and the third from 234 to 205 Ma, both north-younging, may correspond to two phases of slabs roll-back.

Our work focuses on the key region of Yushu (Figure 2), where magmatic rocks and tectonic structures implicated in either of the geodynamic scenarios can be found very close to each others. This gives an unique opportunity to decipher the many tectono-magmatic phases that occurred along the northern Qiangtang margin, although it may however be difficult to achieve accurate correlations between the suture limbs (Reid et al., 2005; Yang et al., 2012).

2.2 Geology of the Yushu mélange and adjacent areas

Around the city of Yushu (Gyêgu), the contact between the North Qiangtang and Songpan-Ganze terranes forms a ~50 km wide domain called either the Yushu *mélange* (Figure 2b, Yang et al., 2012) or the Tongtian River structural belt (*Geological Survey of Qinghai Province*, 1:250 000 Geological Map, 2005). Three lithostratigraphic units have been identified in the Yushu mélange (Yang et al., 2012; Zhang et al., 2017).

The uppermost unit is mainly composed of low-grade metaclastic rocks (slate, phyllite, sandstone) and meta-limestone. Gabbros and pillow basalts with U-Pb zircon ages of c. 236 Ma crop out in this unit as tectonic slivers (B. Liu, Ma, Guo, Xiong, et al., 2016).

The middle unit shows more abundant meta-volcanic rocks (metabasalt, ignimbrites, and ashfall tuff), interbedded with thick-bedded continental metaclastics and meta-limestones. One ignimbrite sample from this unit yielded a U-Pb zircon age of c. 254 Ma (H. Zhang et al., 2017), and an intrusive gabbro dike was dated at c. 258 Ma (B. Liu, Ma, Guo, Sun, et al., 2016). Cross-bedding laminations, ripple marks and plant fragments indicate that the clastic sediments forming the two upper stratigraphic units were deposited in a shallow marine environment (Yang et al., 2012). The contact between these two units was first described as conformable and gradational (Yang et al., 2012), but a more recent work reported instead that the two units were separated by a top-to-the-south high-angle reverse fault (Zhang et al., 2017).

153 The lowermost *Tectonostratigraphic* unit consists of alternating greenschist to blueschist
154 facies metabasalt, marble, metapelite and phengite-bearing volcanodetritic schist (Yang et al.,
155 2012); this study). One gabbroic pluton within this unit yields an U-Pb zircon age of c. 258
156 Ma (Yong et al., 2011; cited in Zhang et al., 2017), but no age data was available for the
157 metabasalts. The two upper stratigraphic units and the lower *Tectonostratigraphic* unit are
158 separated by a north-dipping normal shear zone named the Zhimenda Fault.

159 To the north, the Yushu mélange is juxtaposed with a part of the Songpan-Ganze terrane called
160 the Bayan Har Group turbidites, along the Zhiduo-Xiewu fault. The Bayan Har Group
161 turbidites consist of Middle to Upper Triassic thin-bedded, very fine clastic rocks interbedded
162 with shales, without any volcanic layer (Yang et al., 2012). Provenance studies indicate that
163 these clastic sediments where dominantly sourced from the Qiangtang terrane Paleo-
164 proterozoic basement in the southwest (Jian et al., 2019; K.-J. Zhang et al., 2012). The Bayan
165 Har turbidites are intensely folded and faulted, as they occur within the western extension of
166 the Songpan-Ganze fold-and-thrust belt (Roger et al., 2008). They are intruded by several
167 undeformed elliptic granitoid plutons with zircon U-Pb ages from 212 to 197 Ma (Liu et al.,
168 2019 and ref. therein).

169 South of the Yushu mélange, massive volcanics and volcanodetritic rocks of Late Triassic age
170 form the Yushu arc. Arc rocks are conformably overlain by the Upper Triassic shallow marine
171 strata (bioclastic limestone and clastic rocks) which cover most of the Northeastern Qiangtang
172 block (Yang et al., 2012). At present, the Yushu arc and Yushu mélange are separated by the
173 main segment of the active left-lateral strike-slip Yushu fault (Chevalier et al., 2017; X. Huang
174 et al., 2019) and the Batang River valley alluvium deposits, which conceals the contact.
175 However, elongated granodiorite plutons crop out just north of the Yushu Fault, and nearly
176 parallel to it. With U-Pb zircon ages in the range 215-203 Ma and typical arc geochemical
177 signatures (Roger et al., 2003; Yang et al., 2012; this study), these plutons belong to the Yushu
178 arc. This indicates that the Late Triassic Yushu arc partly intruded the Yushu mélange.

179

180 ## 3. Field Structures and Samples Descriptions of the Yushu Mélange and Adjacent
181 Areas

182

183 In order to examine the lateral continuity of the NW-SE trending structures across the Yushu

arc and mélange, we conducted two c. 25 km-long transects (Figures 2b and 3a,b), northwest (western section AA') and southeast (eastern section BB') of the city of Yushu (Gyêgu/Jiegu). Each cross-section is from the Yushu arc to the *Tectonostratigraphic* unit. In this area, the active left-lateral Yushu fault divides into several branches that cross-cut the transects. The Yushu city valley lies on the main branch, and the two southernmost subordinate branches have a present-day strong normal component (Chevalier et al., 2018; Figure 2b). Three different lithologies were sampled for geochronological analysis: deformed granodiorites, metabasalts and volcanodetritic micaschists. All of the thin-sections described below were cut in the XZ plane of the finite strain (X is parallel to the lineation, and Z is normal to the foliation).

3.1 Western Section (Figure 3a)

3.1.1 Yushu Arc

In the southern part of the western AA' cross-section (Figure 3a), the Yushu arc is represented by a south-to-north succession of deformed coarse-grained conglomerate, massive blueschist-facies basaltic flows and fine-bedded ashes with clasts. To the south of the transect, open folds are overprinted by a pervasive steep NE-dipping schistosity, and top-to-the-south shear planes are locally observed in the beds of ashes. Folds tighten towards the north of the transect, with a NW-SE trending sub-vertical axis planar schistosity, and finally become NE-verging in the vicinity of the Yushu Fault valley.

3.1.2 Mylonitic Pluton

North of the Batang River valley, the *Tectonostratigraphic* unit is intruded by a highly deformed granodioritic pluton, mapped as a NW-SE elongated body of a few tens of kilometers (Figure 2b; *Geological Survey of Qinghai Province*, 1:250 000 Geological Map, 2005). Very fine-grained mylonitic bands define anastomosing sub-vertical shear zones that wrap around elongated lenses of weakly deformed granodiorite (Figure 4a)**.** Some mylonitic bands are biotite-rich, others are quartz and plagioclase-rich with mm-scale garnet porphyroclasts (Figure 5). The main shear direction forms subvertical C_1 planes trending NW-SE (Figure 4a). On these C_1 planes, aligned biotites define a mineral lineation plunging at ~40° to the NW (L_1, Figure 4b), indicative of a lateral component of the deformation, but these planes lack unequivocal shear sense indicators. Some asymmetrical granodiorite lenses suggest top-to-the-SW, dextral displacement along C_1 planes, but most sheared lenses have

symmetrical shapes, suggesting that the deformation of the pluton was dominantly pure shear flattening. The C_1 planes are affected by late sub-horizontal brittle striation, which likely relates to the present-day left-lateral displacement on the neighboring Yushu active fault (Figure 4c). Three samples from this deformed granodiorite (Figure 4a) were selected for $^{40}Ar/^{39}Ar$ and/or U/Pb dating on biotites and zircon respectively: YU-14-68 (weakly deformed granodiorite), YU-14-63b (biotite-rich mylonite band), and YU-14-69 (quartz-plagioclase-garnet mylonite band).

Sample YU-14-68, sampled in the main body of the granodioritic pluton, presents a mineral assemblage of biotite, plagioclase and quartz, with destabilized brown amphibole porphyroclasts, small blue-green amphibole in the foliation, and abundant interstitial oxides (Figure 5a-b). Quartz grains locally coalesce in elongated boudins, giving a slight gneissic layering to the sample. Biotite flakes are only slightly kinked; deformation seems to be mainly accommodated by ductile shear of the quartz boudins.

Sample YU-14-63b, taken from a mylonitic band of the granodiorite pluton, is composed of biotite, plagioclase, quartz and rare alkali feldspar. The thin-section presented in Fig. 5c encompasses both the mylonitic fine-grained domain itself, in which aligned biotites represent 50-60 vol% of the section, and a coarse-grained domain dominated by plagioclase porphyroclasts and elongated quartz boudins, in which biotites are interstitial, either within the foliation or forming pressure shadows of plagioclase. Biotites often have zircon inclusions. Quartz in the coarse-grained domain shows undulatory extinction and migrating grain boundaries (Figure 5d-f), indicative of dislocation creep and dynamic recrystallization mechanisms in a relatively cold deformation regime. Undulatory extinction patterns in quartz and biotite fishes suggest a right-lateral shear on S_1 planes.

Sample YU-14-69, sampled from another mylonite band in the granodiorite pluton, is mainly composed of plagioclase, quartz and alkali feldspar (Figure 5g-h). Quartz either forms small porphyroclasts displaying undulatory extinction and migrating boundaries, or tiny granoblasts in pressure shadows. Biotite grains, in low abundance, define the S_1 foliation plane and show a strong shape preferred orientation that corresponds to the stretching (X) direction. The accessory minerals are white mica, sillimanite and large garnets (1.5 to 2 cm, < 1 vol%). Garnets have atoll textures due to abundant inclusions of rounded quartz and biotite. The symmetric pressure shadows around the garnets, and the lack of clear C-S structures in the whole sample, suggest that deformation in this part of the mylonitic pluton was mainly coaxial. The internal cleavage in the garnet seems to preserve a former foliation that now occurs at a

high angle (~90°) to S_1.

3.1.3 Western *Tectonostratigraphic* unit

Blueschist-facies metabasaltic rocks, mapped as Carboniferous-Permian on the *Geological Survey of Qinghai Province*, 1:250 000 Geological Map (2005), outcrop between the Yushu Fault and the mylonitic granodiorite pluton, at the southern edge of the *Tectonostratigraphic* unit. Glaucophane-zoisite assemblages underline a steep NE-dipping foliation. Greenschist facies metapelites are found structurally above these blueschist-facies metabasalts, showing a shallower N-dipping schistosity with clear top-to-the-north normal shear criteria. One greenschist facies metapelite sample (YU-14-62) was selected for $^{40}Ar/^{39}Ar$ phengite dating, but didn't yield exploitable results because of excess argon (see Results section and Supplementary Table S3).

North of the mylonitic granodiorite pluton, the *Tectonostratigraphic* unit consists in alternations of marbles, blueschist-facies metabasalts and metapelites, affected by SSW-verging overturned folds which transpose the initial bedding, and by ENE-dipping shear planes with clear inverse shear criteria (C_1 on Figure 6b). The C_1 planes bear stretching lineations plunging ~30 to 50°E (Figure 6b), indicating that the top-to-the-WSW thrusting deformation was associated with a significant left-lateral component. One blueschist-facies metabasalt sample (YU-14-64) affected by this transpressive deformation was selected for $^{40}Ar/^{39}Ar$ amphibole dating (Supplementary Table S3). Sampled at the contact with marble, YU-14-64 has a nematoblastic texture, with aggregates of quartz, plagioclase and rare epidote, in a groundmass of acicular blue-green amphibole with strong preferred orientation, interstitial feldspar and secondary calcite (Figure 6c,d). The quartz-plagioclase boudins are folded and transposed into the S_1 foliation (N130°E). One kilometer north of the mylonitic pluton, the blueschist-facies sequence is cross-cut by a subvertical fault zone with a direction similar to that of the C_1 planes (trending ~N130°E with lineation plunging ~40°SE).

Close to the northern boundary of the Tectonostratigraphic unit, the rocks show lower-grade, greenschist facies metamorphism, marble become sparse, and the folded metagreywacke-dominated sequence is intercalated with less deformed variolitic pillow basalts. Conjugate shear directions indicate a dominant flattening deformation on steep E-W striking planes. The contact between the *Tectonostratigraphic* unit and the middle stratigraphic unit of the Yushu mélange is marked by sub-horizontal crenulation folds on NE-dipping planes, which indicate

a normal NE-directed sense of shear, consistent with an exhumation of the higher-grade *Tectonostratigraphic* unit relative to the stratigraphic units (Figure 7). One blueschist-facies metabasalt sample (YU-15-11), sampled in the hangingwall of the Zhimenda fault and affected by this top-to-the-NE normal shear, was selected for $^{40}Ar/^{39}Ar$ dating (Supplementary Table S3).

3.2 Eastern Section (Figure 3b)

3.2.1 Yushu Arc

Just north of the Yushu airport, the carbonate-schist sequences of the Eastern Qiangtang Triassic strata show open upright E-W trending folds with a wavelength of one hundred meters, and a slight top-to-the-north asymmetry (Figure 3b). In the vicinity of the southern limb of the Yushu fault, the shallowly dipping S_0 associated with these open folds is transposed into a WNW-ESE trending sub-vertical fault schistosity. Further north, the carbonates are interlayered with Yushu Arc basalts; both are affected by tight NE-SW trending folds with steep planar schistosity, and cross-cut by moderately dipping top-to-the-NW reverse thrust planes. In the vicinity of the main branch of the Yushu fault, the carbonated rocks become more intensely fractured, with several faulting directions (from N60 to N-S).

3.2.2 Eastern *Tectonostratigraphic* Unit

The eastern hillside of the city of Yushu consists of alternations of volcanoclastic cherts, phyllites and greenschist-facies metabasalts and metagabbros, with a very steep S_0/S_1 schistosity trending ~N100 (Figure 8). These rocks, which we interpret as part of the *Tectonostratigraphic* unit of the Yushu mélange, are affected by top-to-the-NNE shallow-dipping reverse fault planes (Figure 8a-c), with numerous associated kink planes. Muscovite flakes from one reverse fault plane (sample YU-15-07) and biotites from another top-to-the-NNE shear plane (YU-15-09) were sampled for $^{40}Ar/^{39}Ar$ dating (Supplementary Table S3). In thin section, sample YU-15-07 is composed of extremely fine-grained white micas, quartz and oxides (Figure 8d,e). The grain size increases towards the fault plane surface, upon which the white micas were manually picked for the $^{40}Ar/^{39}Ar$ dating. Fish shapes micro-structures show that muscovite porphyroclasts (mus_1 on Fig. 8d-e) were deformed, whereas secondary syn-kinematic muscovites (mus_2 and mus_3) crystallized on the fault plane.

Along the flank of the northern city hillside, where the Yushu monastery stands, the dominant

lithologies are blueschist facies metabasalts and subordinate marbles. The main S_1 foliation planes are oriented ~N100°E and dip sub-vertically (Figure 9a-d). Within the S_1 foliation, shear structures (Figure 9d-f) and isoclinal fold hinges (Fig. 9g,h) are locally observed, suggesting that this S_1 foliation was associated with a first phase of folding and shearing. Shear sense indicators suggest conjugate strike-slip shear planes, compatible with pure shear shortening in the N-S direction (Figure 9e,f). A later phase of deformation is suggested by refolding of the isoclinal P_1 folds by open to tight P_2 folds (Figure 9g,h), with crenulation of the S_1 foliation on P_2 flanks (Figure 9i). The S_1/C_1 structures are also affected by top-to-the-NE shear planes (Fig. 9a-d). Two folded blueschist-facies metabasalt samples (YU-15-16 and YU-15-17) were collected for $^{40}Ar/^{39}Ar$ dating (Supplementary Table S3).

Further east, towards the Zhimenda fault, the rocks show lower-grade metamorphism, similarly to what observed in the western transect. The main foliation planes dip more shallowly to the NE (<30°) and bear shallow-plunging stretching lineation indicating left-lateral top-W reverse shear. One biotite schist sample (YU-15-06), affected by this left-lateral deformation, and one greenschist facies metabasalt sample (YU-15-05) were collected for $^{40}Ar/^{39}Ar$ dating (Supplementary Table S3).

3.3 The Zhiduo-Xiewu Fault Zone

Structural analysis was also carried in the Zhiduo-Xiewu fault zone, northwest of the city of Yushu, in order to better characterize this major contact between the Qiangtang and Songpan-Ganze terranes. We identified a landscape-scale SSW-dipping fault that could be traced for hundreds of meters on both sides of the river. This top-to-the-north reverse fault juxtaposes the northward-fining sandstone sequence of the uppermost stratigraphic unit of the Yushu mélange, above the very fine-bedded micaceous slates of the Bayan Har turbidites (Figure 10). The Zhiduo-Xiewu fault corresponds to a top-to-the-north thrust of the Yushu mélange above the Songpan-Ganze Triassic formations. One fine-grained sandstone sample from the hanging wall (YU-15-19), and one slate sample from the footwall (YU-15-20), were collected for $^{40}Ar/^{39}Ar$ dating (Supplementary Table S3).

4. Analytical Methods

4.1 Zircon U-Pb Dating

The rock sample was crushed using standard procedures. The zircon grains were handpicked from the 80-200 micrometer non-magnetic fraction, placed on epoxy mounts and polished.

Back-scattered electron images of the grains were acquired with a Hitachi S2500 Scanning Electron Microprobe at the Institut des Sciences de la Terre (ISTerre) of Grenoble (France). U-Pb zircon analyses were performed by in-situ LA-ICP-MS, using an ESI NWR193UC excimer laser coupled to a quadrupole Agilent 7700x ICP-MS at the GeOHeLiS analytical Platform (OSUR, Univ. Rennes). The diameter of the ablation spots varies from 20 to 30 µm, depending on the grain size. The repetition rate of the ablation was 3 Hz. Data were corrected for U-Pb and Th-Pb fractionation and for mass bias by repeated measurements of the standard GJ-1 (Jackson et al., 2004). Accuracy was monitored by analyses of the standard Plešovice (337.13 ± 0.37 Ma, Sláma et al., 2008), which produced a concordia age of 337.1 ± 2.1 Ma (N=18; MSWD=0.65) during the course of the analyses. Data reduction was carried out using the software Iolite v4 (Paton et al., 2010, 2011). The concordia ages and diagrams were generated using IsoplotR (Vermeesch, 2018). The full instrumental and analytical conditions can be found in Supplementary Table S2 and in Nosenzo et al. (2022)

4.2 $^{40}Ar/^{39}Ar$ Dating

4.2.1 $^{40}Ar/^{39}Ar$ data extraction

Rock samples were crushed using standard procedures. Individual grains were handpicked from the 0.5-1-millimeter fraction of the crushed samples. Samples were irradiated in three batches, IR24, IR26 and IR36, at McMaster Nuclear Reactor (Hamilton, Ontario, Canada - http://www.science.mc master.ca/mnr/) in its 8E high neutron flux facility. IR24 IR26 and IR36 lasted 50.967h, 50h and 200.95h with global efficiencies (J/h) of 4.97 x 10^{-5}, 8.25 x 10^{-5} h^{-1} and 1.03 x 10^{-4} h^{-1}.

The analytical procedure is described by (Ruffet et al., 1991, 1995). The irradiation standard were sanidine TCRs (28.608 ± 0.033 Ma according to (Renne et al., 1998, 2010, 2011) for irradiation IR24 and IR26 and amphibole Hb3gr (Jourdan et al., 2006; Jourdan & Renne, 2007; Roddick, 1983; Turner, 1971); 1081.0 ± 1.2 Ma according to (Renne et al., 2010, 2011) for irradiation IR36. Blanks were performed routinely each first or third/fourth run, and are subtracted from the subsequent sample gas fractions. Errors of apparent ages are plotted at the 1σ level and do not include the errors on the $^{40}Ar^*/^{39}Ar_K$ ratio and age of the monitor and decay constant. Plateau ages were calculated if 70% or more of the $^{39}Ar_K$ was released in at least three or more contiguous steps which define apparent ages agreeing, to within 2σ, with the integrated age of the plateau segment. This 70% threshold, a requirement criterion that we use in all our geochronological studies (e.g. (Perrot et al., 2020), is much more restrictive than the 50% threshold set subjectively, in their own words, by (Fleck et al., 1977) and still adopted by most

of the users of the $^{40}Ar/^{39}Ar$ method. On the other hand, as the the amount of $^{39}Ar_K$ released is not a disqualifying criterion, we have for a long time associated to our restrictive age plateau concept (≥ 70% of $^{39}Ar_K$) used for "simple" mineral phases, the concept of pseudo-plateau (Cheilletz et al., 1999) which meets the same statistical criteria except for the cut-off threshold (<70% of $^{39}Ar_K$), and which is much more efficient for the analysis of complex mineral phases. We also use a plateau-like descriptive terminology which refers to a weighted average age calculated over a segment of apparent ages considered to be geologically significant.

The errors on the $^{40}Ar^*/^{39}Ar_K$ ratio and age of the monitor and decay constant are included in the final calculation of the error margins on the pseudo-plateau and plateau ages. $^{40}Ar/^{39}Ar$ ages are provided with 2σ errors. Analytical data and parameters used for calculations (e.g. isotopic ratios measured on pure K and Ca salts; mass discrimination; atmospheric argon ratios; J parameter; decay constants) and reference sources are available in the Supplementary Table S3.

4.2.2 $^{40}Ar/^{39}Ar$ data processing

Minerals from deformed rocks are usually texturally complex (recrystallized, composite grains, etc). The $^{40}Ar/^{39}Ar$ analyses of such materials is useful, as information it provides integrates the effects of the disturbing processes and therefore the timing of their occurrence (e.g. Castonguay et al., 2007; Cheilletz et al., 1999; Daoudene et al., 2022; Hames et al., 2008; Tremblay et al., 2020). Hence, due to the complexity of $^{40}Ar/^{39}Ar$ results that arise from the analysis of such materials, their processing must go beyond the simple visual examination of age spectra. (De Putter et al., 2015; De Putter & Ruffet, 2020; Tremblay et al., 2020) presented and developed tools for the visualization and processing of complex $^{40}Ar/^{39}Ar$ systems. Of these, two of them are atypical, the degassing and the weighted age spectra, which were designed to visualize Ar degassing kinetics of $^{40}Ar/^{39}Ar$ experiments to highlight secondary components. As a reminder, $^{37}Ar_{Ca}/^{39}Ar_K$ spectra transcribe the evolution of the Ca/K ratio ($^{37}Ar_{Ca}$ # Ca and $^{39}Ar_K$ # K with $^{37}Ar_{Ca}/^{39}Ar_K = CaO/K_2O$ / 2.179; (Deckart et al., 1997) during step-heating (degassing) experiments.

5. Results

5.1 Zircon U-Pb Data

One sample (YU-14-63b) from the mylonite facies of the granodiorite pluton that intrudes the tectonostratigraphic unit was dated by U-Pb on zircon. 68 single spot in-situ analyses were conducted on a total of 26 different grains. The analyzed grains show variable morphologies (Figure 11a): some are subhedral with bright oscillatory zoning, others are rounded with resorbed cores and complex, irregular zoning patterns, while two rounded grains lack any zonation. Pb and U contents are highly variable between 21-9621 ppm and 99-13017 ppm, with a mean Th/U ratio of 0.43 (varying from 0.02 to 4.0; Supplementary Table S1). There is no correlation between the U/Th ratios and the corresponding apparent ages.

20 analyses (in italic and red in Supplementary Table S1) yield a significant amount of common Pb and will therefore not be discussed further. Three discordant analyses of inherited cores give Proterozoic $^{207}Pb/^{206}Pb$ apparent ages of 1983 ± 18 Ma, 1823 ± 77 Ma and 1723 ± 36 Ma respectively. A set comprising the 30 oldest analyses measured on 19 different grains yield a Late Triassic concordia date of 213.6 ± 1.5 Ma (MSWD=1.8; Figure 11c and Supplementary Table S1), date equivalent within error with a mean $^{206}Pb/^{238}U$ date of 210.3 ± 1.2 Ma (MSWD=0.9). In most grains, spot analyses on the outer rims yield apparent U-Pb ages younger than the inner rims and cores (Figure 11a). Together, these 15 analyses yield a mean $^{206}Pb/^{238}U$ date of 199.5 ± 1.7 Ma (MSWD=0.4; Figure 11f and Supplementary Table S1), which is equivalent within error with a concordia date of 203.4 ± 2.4 Ma (MSWD=2.4, Figure 11d). The signification of this date will be discussed in section 6.2.

5.2 $^{40}Ar/^{39}Ar$ Data

15 samples were investigated by the $^{40}Ar/^{39}Ar$ method, for a total of 23 analyses of individual white micas, biotites, amphiboles and whole rocks grains, of which 7 are duplicates. The results are presented in Figure 12. These analyses reveal at least 3 distinct periods, from the Early Triassic to the Early Jurassic, which could have been followed by a latter one in the Middle Jurassic.

Two samples, a greenschist-facies metapelite (YU-14-62) with two white mica grains, and a blueschist-facies metabasalt (YU-15-16) with a glaucophane and two whole-rock grains yielded anomalous and unusable results. The anomalously old apparent ages of the white micas from the metapelite could suggest trapping of argon in excess, or more likely reflect a detrital origin partially preserved during greenschist metamorphism. The extremely low K content of the

metabasalt and of its sodic amphibole makes them unsuitable material for $^{40}Ar/^{39}Ar$ experiments.

The oldest radiogenic component, Early Triassic in age, is evidenced by the whole rock sample YU-15-11. This blueschist facies metabasalt is the northernmost sample from the tectonostratigraphic unit. The high-temperature steps in its age spectrum, together with a specific degassing peak, allow calculating a pseudo-plateau age at 252.7 ± 1.2 Ma. The low-temperature degassing domain of this sample does not allow to identify a radiogenic component that could explain the small inflection observed in the medium-temperature degassing domain.

Nonetheless, this study clearly highlights at least two younger radiogenic components. The first, Late Triassic, appears to be polyphased as suggested by both the mylonitic (YU-14-63b) and the weakly deformed (YU-14-68) facies of the granodiorite that intrudes the tectonostratigraphic unit. One of the two biotites of the weakly deformed facies provides a plateau age at 217.9 ± 1.0 Ma in the high degassing temperature domain preceded in the low temperature steps by a pseudo-plateau at 212.7 ± 2.2 Ma, which is associated with a well individualized degassing peak with a strong impact on the weighted age spectrum (De Putter et al., 2015; De Putter & Ruffet, 2020; Tremblay et al., 2020). This peak indicates that the related radiogenic component is hosted by a crystal component distinct from that of the older main radiogenic component, probably related to recrystallization or neo-crystallization (e.g. (Tremblay et al., 2020). In detail, apparent ages of this age spectrum increase steadily from c. 212.7 Ma in the low temperature domain to c. 219.2 Ma at grain fusion. The apparent ages of the age spectrum of the second biotite from sample YU-14-68 also increase steadily during degassing, but from c. 196.1 Ma, as will be discussed later, to c. 209.1 Ma. The two biotites of the mylonitic facies of the granodiorite provide results perfectly consistent with those of the undeformed facies. The first one allows the calculation of a plateau age at 214.6 ± 0.8 Ma. The apparent ages of the age spectrum of the second one increase steadily during degassing, from c. 214.6 Ma in the low temperature domain to c. 219.3 Ma at the end of the experiment. The low-temperature domain is dominated by a consistent degassing peak with a strong impact in the weighted age spectrum that highlights a physically well individualized radiogenic component that developed after a radiogenic component at least as old as c. 219 Ma.

The white mica YU-15-07, collected on a top-to-the-NNE reverse fault plane, depicts a similar, protracted and discontinuous history. The saddle shape of its age spectrum is characteristic of the coexistence of two radiogenic components of distinct ages within the analyzed mineral, which reflect a partial recrystallization, probably related to continuous deformation and fluids

(e.g. (Alexandrov et al., 2002; Castonguay et al., 2007; Cheilletz et al., 1999; Tartese et al., 2011; Tremblay et al., 2011, 2020). It occurred at the earliest at 213.5 ± 1.1 Ma at the expense of a mineral at least as old as 216.8 ± 0.9 Ma. A sericitized biotite (YU-15-09) collected from a similar structure provided an age spectrum with significantly younger apparent ages. Its shape does not allow to deduce any relevant information.

Two metabasalts from the tectonostratigraphic unit also hold this Late Triassic radiogenic component. The whole rock YU-15-05 reveals it in the high-temperature domain, in connection with the degassing of a calcium-rich component as shown by the $^{37}Ar_{Ca}/^{39}Ar_{K}$ spectrum. This high-temperature segment allows calculating a pseudo-plateau age of 214.5 ± 4.0 Ma. Similarly, one of the amphiboles in sample YU-14-64 shows this Late Triassic radiogenic component in the middle domain of its age spectrum, related to its main degassing as indicated by its degassing spectrum. The flat segment identified in the age spectrum, with a mean $^{37}Ar_{Ca}/^{39}Ar_{K}$ ratio at c. 7.5, allows calculating a pseudo-plateau age at 215.4 ± 1.0 Ma. The age spectrum of this amphibole suggests that the Late Triassic radiogenic component is of secondary origin and would result from the partial recrystallization of a more calcic amphibole, as suggested by the $^{37}Ar_{Ca}/^{39}Ar_{K}$ ratio of c. 11 of the mineral's fusion step, which would be at least as old as c. 239 Ma. The degassing spectrum also identifies a low-temperature degassing peak linked to a small flat segment in the age spectrum that characterizes an early Jurassic component. This segment, which defines a pseudo-plateau at 187.6 ± 1.9 Ma, is clearly discernible in the weighted age spectrum. This expresses the degassing of a radiogenic component physically distinct from that of the Late Triassic. This Early Jurassic component is also apparent in the age spectrum of the second amphibole, with 3 apparent ages that define a pseudo-plateau at 191.6 ± 1.2 Ma. It is revealed in the degassing spectrum by an evasive hump which overlaps the degassing domain of the Early Triassic component, likely the reason why the latter is expressed with a younger age at c. 203.7 Ma.

The Early Jurassic radiogenic component recorded as a disturbance by the amphiboles of the YU-14-64 metabasalt is the only radiogenic component recorded by the biotites of the felsic mylonite band (YU-15-69) sampled in the granodiorite. The two biotites provide two slightly discordant plateau ages at 197.2 ± 0.8 Ma and 193.6 ± 0.9 Ma. Examination in detail of the oldest age spectrum shows that apparent ages increase steadily during degassing of the mineral from 192.4 ± 2.8 Ma to 202.6 ± 4.4 Ma at the fusion step. The plateau age at c. 197 Ma for this biotite would be an artefact. This age spectrum expresses an incomplete reset of the mineral during the Early Jurassic event, when it had initially crystallized or recrystallized during the Late Triassic event. A similar process was probably at work for the biotite YU-14-68 which

provided younger apparent ages than its duplicate and whose age spectrum shape was discussed earlier.

The two samples collected 22 km north of Yushu town in the hangingwall (YU-15-19) and footwall (YU-15-20) of the SSW-dipping Zhiduo-Xiewu fault zone provided two similar age spectra. They are characterized by flat segments in the low degassing temperature domain, with perfectly matching pseudo-plateau ages at 201.3 ± 1.0 Ma and 201.4 ± 0.8 Ma for $^{37}Ar_{Ca}/^{39}Ar_{K}$ ratios at c. 0.004, and continue with apparent ages that increase until the end of the experiment, e.g. c. 272 Ma for YU-15-20, concomitant with $^{37}Ar_{Ca}/^{39}Ar_{K}$ ratios (c. 0.1-1). The two low temperature pseudo-plateaus are linked to specific degassing peaks that suggest the development, by recrystallization, of physically well individualized potassic radiogenic components at the expense of older (>c. 270 Ma) and more calcic ones.

The existence of a Middle Jurassic age event could be assumed on the basis of the ages produced by the biotite and whole rock age spectra of the biotite-schist sample YU-15-06. The pseudo-plateau age at 173.9 ± 1.3 Ma in the high temperature steps of the biotite age spectrum seems to be supported by the high temperature segment of the whole rock age spectrum. However, it may only reflect incomplete resetting of the biotite by volume diffusion during a thermal event as suggested by the shape of the age spectrum (Turner, 1968). This loss of $^{40}Ar^{*}$ could have occurred during a significantly younger event, around c. 165 Ma, as suggested in the low temperature domain by the apparent ages in the biotite age spectrum and the peak discernible in the whole rock degassing spectrum.

Figure 13 summarizes the results presented above against the frequency histogram (probability density diagram) of apparent ages (Deino & Potts, 1992). The samples are classified according to their sampling distance from the Zhiduo-Xiewu Fault. Three main periods are identified. The oldest period, identified on the northernmost sample of the tectonostratigraphic unit, is thought to be of Early Triassic age (c. 247.1-253.9 Ma). The main period detected in this $^{40}Ar/^{39}Ar$ geochronological analysis is of Late Triassic age and appears to be polyphased with 2 distinct sub-periods, a first one around 215.9-221.4 Ma which appears to be partially reworked during a second one around 210.5-216.3 Ma. The Late Triassic period is identified in the southern domain of the *tectonostratigraphic unit*. While this Late Triassic event is recorded there as a post-Early Triassic disturbance of blueschist-facies metabasalts, it is apparently the oldest phase recorded in the mylonitised granodiorite samples, which suggests that the intrusion of this pluton was syntectonic and occurred concurrently with a period of Top-to-the-NNE reverse faulting activity. In contrast, samples from the Zhiduo-Xiewu fault zone record a significantly

younger period of activity, at the Triassic-Jurassic transition (c. 200-202 Ma). A third period of activity is recorded in the southern domain of the tectonostratigraphic unit. It is thought to be of early Jurassic age (190.4-194.5 Ma). It impacts both the metabasalts of the *tectonometamorphic* unit and the mylonitized pluton but without any recorded repercussions on the Top-to-the-NNE reverse faults. The last event suspected in this study could be of Middle Jurassic age (159.7-168.6 Ma).

6. Discussion

6.1 Deformation styles in the *Tectonostratigraphic* unit

Our observations from the *Tectonostratigraphic* unit in the surroundings of Yushu city (cross-section BB') are in good agreement with the works of Yang et al., (2012): while the micaschists and greenschist-facies basalts sequences mainly record asymmetric top-to-the-north faulting (Figure 8), the blueschist-facies metabasaltic rocks also present evidences of coaxial shortening, with conjugate shear planes and refolding of early transposed S_1/C_1 fabrics by more open P_2 folds (Figure 9). Moreover, within the mylonitic granodiorite pluton we studied west of Yushu city (cross-section AA'), the anastomosing mylonitic shear zones show no evident shear sense criteria (Figure 4), and both pure and simple shear are observed at microscopic scale on the mylonite bands (Figure 5). This suggests that deformation was accommodated by both right- and left-lateral displacements on the subvertical C_1 planes, resulting in coaxial flattening of the pluton.

By contrast, in the blueschist-facies metabasalt-marble alternations from the western *Tectonostratigraphic* unit (cross-section AA'), as well as in chlorite-biotite schists from the eastern part of the *Tectonostratigraphic* unit (sample site of YU-15-06), the systematic presence of moderately plunging ductile lineations on C_1 shear planes, combined with shear sense indicators, consistently indicate that top-to-the-WSW thrusting was accompanied by an important left-lateral component. This transpressive ductile deformation is distinct from the brittle and purely strike-slip or normal faulting related to the present-day activity of the Yushu fault.

Based on their $^{40}Ar/^{39}Ar$ thermochronology data, Yang et al., (2012) proposed that top-N shearing started at c. 230 Ma, and that compression progressively oriented N-S from 215 to 190 Ma. Our new $^{40}Ar/^{39}Ar$ results, combined with previous studies carried in the Yushu and

Zhiduo areas, precise and extend our knowledge about the deformation history of the Yushu area.

6.2 Origin of the Earliest Deformation of the Yushu mélange

New $^{40}Ar/^{39}Ar$ data unravel a previously unrecognized early phase of deformation in the Yushu mélange. A metabasalt sampled in the hangingwall of the Zhimenda fault which separates the *Tectonostratigraphic* and stratigraphic units, affected by unambiguous normal shear, provided an $^{40}Ar/^{39}Ar$ pseudo-plateau age at 252.7 ± 1.2 Ma (sample YU-15-11, Figure 12). This suggests that the Yushu mélange recorded extensional tectonics during Permo-Triassic times.

This period corresponds to the emplacement of c. 258-254 Ma gabbros and basalts within the *Tectonostratigraphic* and middle stratigraphic units of the Yushu *mélange* (Figure 2b; Liu et al., 2016; Zhang et al., 2017), which present back-arc geochemical affinities and stratigraphic signatures (e.g. a lack of associated marine sedimentation). Since this period also correlates with the magmatic flare-up of the Zhaduo arc at c. 275-248 Ma (Yang et al., 2011), the Yushu *mélange* likely represents the former back-arc basin of a northward subduction along the Longmu Co-Shuanghu suture, as previously suggested by Yang et al. (2012) (Figure 14a).

A phengite schist from the hangingwall of the Zhimenda normal fault provided a younger $^{40}Ar/^{39}Ar$ plateau age of c. 230 Ma (Yang et al., 2012; Figure 2b). This suggests that the extensional tectonic regime could have lasted until (or resumed in) the beginning of the Late Triassic. Indeed, Middle Triassic gabbros and basalts dated at 234-236 Ma crop out within the upper stratigraphic unit (Figure 2b; Liu et al., 2016). They also present a back-arc geochemical affinity, although not as clear as the Permian mafic rocks (both E-MORB and OIB signatures are present). This period also corresponds with eclogite peak metamorphism at c. 233 Ma on the Longmu Co-Shuanghu suture (Dan et al., 2018; Q.-G. Zhai et al., 2011). This could indicate that the Yushu back-arc was active during all the life span of the Longmu Co-Shuanghu subduction, from the Late Permian to the Middle Triassic (Figure 14b).

6.3 Late Triassic Syn-Magmatic Deformation in the Yushu mélange

Numerous high-quality zircon U-Pb geochronological data have been published to constrain

598 the timing of magmatism in the Yushu-Zhiduo area (Chen et al., 2005; Gu et al., 2013; Jin,
599 2006; G.-M. Li et al., 2015; J. Li et al., 2012; B. Liu, Ma, Guo, Sun, et al., 2016; B. Liu, Ma,
600 Guo, Xiong, et al., 2016; Yan Liu et al., 2019; Yin Liu et al., 2010, 2014, 2019, 2021; Tan et
601 al., 2020; B. Z. Wang et al., 2008; Yang et al., 2012; Yong et al., 2011; H. Zhang et al., 2017;
602 Zhao, Fu, et al., 2015; Zhao, Tan, et al., 2015). Our zircon U-Pb concordia date of 213.6 ± 1.5
603 Ma obtained for the mylonitic granodiorite (sample YU-14-63b, Figure 11) is perfectly
604 consistent with the emplacement age previously obtained for the other granodiorite pluton east
605 of Yushu city (214.5 ± 1.4 Ma; Yang et al., 2012) , whereas the elongated diorite plutons in
606 the Zhiduo area, further northwest, provided slightly older emplacement ages of 216 ± 1 Ma
607 and 218 ± 1 Ma (B. Z. Wang et al., 2008; Zhao, Fu, et al., 2015). All these granodiorite plutons
608 were emplaced during the latest stages of Late Triassic arc magmatism along the northern
609 Qiangtang margin (the Zhiduo-Yushu-Yidun arc), coevally with the 221-213 Ma North
610 Zhiduo volcanic belt (Figure 2a; (Yan Liu et al., 2019).

611 Our $^{40}Ar/^{39}Ar$ geochronological data provide more details about the emplacement and early
612 evolution of the granodiorite plutons. One biotite from the granodiorite sample (YU-14-63b)
613 yields an $^{40}Ar/^{39}Ar$ plateau age identical within error (214.6 ± 0.8 Ma) to its zircon U-Pb
614 concordia age (Figure 12). Surprisingly, other biotites from the granodiorite pluton yield older
615 plateau age of c. 217 Ma and/or high-temperature apparent ages of 219 Ma. Detailed analyses
616 of their spectra suggest that these biotites crystallized at c. 219 Ma and were subsequently
617 disturbed at 214-212 Ma. This could indicate that the granodiorite pluton was fed with magma
618 from c. 219 to c. 213 Ma, and that shearing started before final cooling.

619 The period c. 213-215 Ma is also recorded as a time of disturbance in three other deformed
620 samples from the *Tectonostratigraphic* unit: two metabasalts samples affected by top-to-the-
621 WSW transpressive shear (one amphibole from sample YU-14-64, and the whole-rock
622 fraction from sample YU-15-05), and the top-to-the-NNE reverse fault plane in micaschists
623 (sample YU-15-07) (Figures 12 & 13).

624 Late Triassic arc magmatism in the Yushu region was thus coeval with a main phase of
625 deformation in the *Tectonostratigraphic* unit of the Yushu mélange. This deformation event
626 is marked at the same time by syn-magmatic subvertical shearing of the plutonic rocks of the
627 Yushu-Zhiduo arc, southwestward ductile transpression in the high-grade rocks, and
628 northeastward thrusting in the volcanoclastic schists.

629 This Late Triassic tectono-magmatic event is consistent with the southward subduction of the

Songpan-Ganze Ocean along the western Jinsha and Ganze-Litang sutures (Figure 14c; (Reid et al., 2005; Yang et al., 2014): the north-verging thrusts and kink planes observed in volcanoclastic schists of the western Yushu *mélange* (Figure 7) indeed correspond to the expected deformation in an accretionary prism associated to a south-verging subduction. With this subduction polarity, we propose that the top-to-the-WSW, left-lateral shear planes observed in the blueschist sequences of the western Yushu *mélange* (Figure 6) could represent the transpressive back-thrusts of a positive flower structure (Figure 3c) in a context of oblique convergence between the Songpan-Ganze and Qiangtang terranes (Figure 14c). This tectonic context is comparable to the Late Triassic Iran-Asia collision (Zanchi et al., 2016). It is also possible that during the Late Triassic, the deformations associated to two convergent Paleo-Tethyan subduction systems (see section 2.1) may have overlapped in the Yushu mélange. In fact, eclogite-facies metamorphism along the Longmu Co-Shuanghu suture indeed yields U-Pb ages as young as 223 Ma in the Baqing area (sZhang et al., 2018); and considering the apparent eastward-younging trend of metamorphic ages along the suture, these authors further proposed that convergence along the Longmu Co-Shuanghu suture could have been counterclockwise(Zhai et al., 2011).

6.4 A Distinct Early Jurassic Phase of the Deformation

Our new $^{40}Ar/^{39}Ar$ geochronological data from the Zhiduo-Xiewu fault indicate that top-NNE thrusting of the Yushu mélange above the Bayan Har group turbidites occurred at ca. 201 Ma (Figure 13). This result precisely constrains the collision of the Qiangtang and Songpan-Ganze terranes, following the final closure of the Paleo-Tethys along the Western-Jinsha and Ganze-Litang sutures.

Within the *Tectonostratigraphic* unit, an Early Jurassic event is well recorded in the geochronological data of the granodiorite plutons, but also in deformed metabasalts. In the deformed granodiorite pluton, zircon rims provided a mean $^{206}Pb/^{238}U$ age of 199.5 ± 1.7 Ma (Figure 11f). A biotite from the granodiorite provided an $^{40}Ar/^{39}Ar$ plateau age of ca. 193 Ma (Figure 13). This sample (YU-14-69) is characterized by a more distinctly coaxial deformation (see section 3.1.2). Another mylonitized granodiorite pluton east of the Yushu yielded comparable muscovite $^{40}Ar/^{39}Ar$ plateau ages of c. 193-195 Ma (Yang et al., 2012). $^{40}Ar/^{39}Ar$ data indicate that some granodiorite biotites (YU-14-69 & YU-14-68) (re)crystallized at ca. 196-192 Ma and that amphiboles from metabasalt sample YU-14-64 were disturbed at ca. 187

and 191 Ma (Figure 13).

These ages suggest that after the Late(st) Triassic collision of the Qiangtang and Songpan-Ganze terranes at ca. 201 Ma, the deformation propagated southward to the *Tectonostratigraphic* unit of the Yushu mélange in the Early Jurassic, where it produced mainly coaxial shortening ("P_2" phase of Yang et al., 2012; Figure 14d). The growth of zircon rims and (re)crystallization of biotites suggest that this Early Jurassic collisional deformation occurred within an elevated thermal regime. It is indeed coeval with the emplacement and metamorphism of collisional granitoids in the adjacent Songpan-Ganze terrane (Liu et al., 2019; de Sigoyer et al., 2014; and ref. therein). Considering the Middle Jurassic disturbances detected in the $^{40}Ar/^{39}Ar$ spectra of metabasalt YU-15-06, it is possible that this late shortening phase lasted until c. 174 Ma or even c. 165 Ma.

6.5 Absence of Cenozoic High-Temperature Reactivation of the Jinsha Suture

Our new $^{40}Ar/^{39}Ar$ ages indicate that the Western Jinsha suture in the Yushu area did not experience high- or medium-temperature deformation during the Cenozoic: the youngest ages obtained are Middle Jurassic. At first glance, the Western Jinsha suture thus behaved passively during the regional Eocene upper-crustal shortening, as a fossil suture zone (Figure 14e). This apparent lack of Cenozoic deformation on this major inherited Mesozoic structure contrasts with the strong (up to 100 km) Cenozoic shortening of the Yushu-Nangqian fold-and-thrust belt, just south of our study area (~40% shortening from >51 Ma to c.37 Ma; Spurlin et al., 2005), and of the Fenghuo Shan fold-and-thrust belt, which straddles the Western Jinsha suture (~24% shortening from c. 45 to 27 Ma; Staisch et al., 2016). In fact, if any post-Jurassic deformation occurred in our study area, it was certainly at temperatures that were too low to be recorded by the K-Ar isotopic chronometers used in this study. Indeed, in the Fenghuo Shan fold-and-thrust belt, multiple low-temperature geochronometers had to be used to determine the Eocene deformation ages: $^{40}Ar/^{39}Ar$ fault gouge illite dating, with closure temperatures of ~280°C, and apatite U-Th/He dating and fission track (AFT) counting, with closure temperatures of ~120-200°C (Staisch et al., 2016). As another example, in the nearby Longmen Shan area, a previously unrecognized Early Cretaceous phase of the deformation was constrained by in-situ dating of metamorphic white micas crystallized under greenschist facies temperatures of 280°C (Airaghi et al., 2017). More generally, the Tibetan Plateau as a whole is characterized by little or no resetting of mid-temperature geochronometers following Jurassic times (Jolivet, 2017; Rohrmann et al., 2012), and thus by a scarcity of Cenozoic

thermochronological data recording post-collisional crustal thickening. This is partly due to the limited erosion linked to tectonic processes, which prevents deep rocks from being exhumed (Guillot et al., 2019). As a result, the use of multiple low-temperature dating methods could be a promising way to unravel the full deformation history of the Jinsha suture since the Early Jurassic. In any case, the lack of high- and mid-temperature reactivation of the Jinsha suture questions the Cenozoic intra-continental subduction model (Guillot & Replumaz, 2013; Replumaz et al., 2016; Tapponnier et al., 2001), and indicates that this model needs to be refined. We have shown that the Yushu mélange accommodated convergence (subduction then collision) from the Late Triassic to the Middle Jurassic. Part of the crustal thickening associated with this protracted convergence may have been preserved until the Cenozoic, and may participate to the present-day total crustal thickness of the northern Tibetan Plateau (70 km in northern Qiangtang). This is supported by paleoaltimetric studies in the Yushu area, which have reported close-to-present elevations as early as the Paleocene-Eocene (Rohrmann et al. in Hetényi et al., 2018; Li et al., 2018; Zhang et al., 2019).

7. Conclusion

New deformational ages obtained in the Yushu area, and a compilation of the sparse existing data from the Western Jinsha suture, show that this region in northeastern Qiangtang was affected by three main tectono-magmatic events between the Early Triassic and the Early Jurassic. First, the opening and expansion of a back-arc basin related to the northward subduction of the Paleo-Tethys along the Longmu Co-Shuanghu suture is recorded from ca. 253 to 230 Ma. Then, the southward subduction of the Songpan-Ganze Ocean along the Western Jinsha suture culminated ca. 219-213 with the syn-tectonic emplacement of many granodiorite plutons along the northern Qiangtang margin. Finally, deformation ended at ca. 201 Ma with the collision of the Qiangtang and Songpan-Ganze terranes. Coaxial shortening related to this collision propagated southward in the Early Jurassic (ca. 196-187 Ma) where it may have lasted until the Middle Jurassic (ca. 165 Ma). In contrast, no evidence for any high- or mid-temperature Cenozoic reactivation of the Jinsha suture is found in this study area.

Data availability statement

U-Pb and K-Ar isotopy data (Supplementary Tables S1 and S3) are currently being

archived in the PANGAEA database (https://pangaea.de/?t=Lithosphere). All data and analytical conditions can be found in the supporting information.

Acknowledgements

This project was funded by the Agence Nationale de la Recherche (ANR-13-BS06-012-01) and the Labex OSUG@2020 (ANR10 LABX56). GDN acknowledges funding from ERC grant MAGIC 649081. The editor Laurent Jolivet and two anonymous reviewers are warmly acknowledged for their detailed and constructive suggestions that helped to improve the manuscript.

References

Airaghi, L., de Sigoyer, J., Lanari, P., Guillot, S., Vidal, O., Monié, P., et al. (2017). Total exhumation across the Beichuan fault in the Longmen Shan (eastern Tibetan plateau, China): Constraints from petrology and thermobarometry. *Journal of Asian Earth Sciences*, *140*, 108–121. https://doi.org/10.1016/j.jseaes.2017.04.003

Alexandrov, P., Ruffet, G., & Cheilletz, A. (2002). Muscovite recrystallization and saddle-shaped 40 Ar/ 39 Ar age spectra: example from the Blond granite (Massif Central, France). *Geochimica et Cosmochimica Acta*, *66*(10), 1793–1807. https://doi.org/10.1016/S0016-7037(01)00895-X

Castonguay, S., Ruffet, G., & Tremblay, A. (2007). Dating polyphase deformation across low-grade metamorphic belts: An example based on 40Ar/39Ar muscovite age constraints from the southern Quebec Appalachians, Canada. *Geological Society of America Bulletin*, *119*(7–8), 978–992.

Cheilletz, A., Ruffet, G., Marignac, C., Kolli, O., Gasquet, D., Féraud, G., & Bouillin, J. P. (1999). 40Ar/39Ar dating of shear zones in the Variscan basement of Greater Kabylia (Algeria). Evidence of an Eo-Alpine event at 128 Ma (Hauterivian–Barremian boundary): geodynamic consequences. *Tectonophysics*, *306*(1), 97–116.

Chen, W., Zhang, Y., Chen, K. L., Zhang, X. T., Wang, Q. L., & Jin, G. S. (2005). Tectonic discrimination and 40Ar/39Ar geochronology of Haxiu quartz diorite in Yushu, Qinghai Province [in Chinese with English abstract]. *Acta Petrologica et Mineralogica*, *24*, 393–396.

Chevalier, M.-L., Leloup, P. H., Replumaz, A., Pan, J., Métois, M., & Li, H. (2018). Temporally constant slip rate along the Ganzi fault, NW Xianshuihe fault system, eastern Tibet. *GSA Bulletin*, *130*(3–4), 396–410. https://doi.org/10.1130/B31691.1

Dan, W., Wang, Q., White, W. M., Zhang, X.-Z., Tang, G.-J., Jiang, Z.-Q., et al. (2018). Rapid formation of eclogites during a nearly closed ocean: Revisiting the Pianshishan eclogite in Qiangtang, central Tibetan Plateau. *Chemical Geology*, *477*, 112–122. https://doi.org/10.1016/j.chemgeo.2017.12.012

764 Daoudene, Y., Tremblay, A., Ruffet, G., & Leclerc, F. (2022). The Abitibi-Opatica
765 transition, Superior Province, Quebec, Canada: structural analysis, 40Ar/39Ar
766 thermochronology and implications for Archean tectonics. *Precambrian Research*, *379*,
767 106803.

768 De Putter, T., & Ruffet, G. (2020). Supergene manganese ore records 75 Myr-long
769 Campanian to Pleistocene geodynamic evolution and weathering history of the Central
770 African Great Lakes Region–Tectonics drives, climate assists. *Gondwana Research*, *83*, 96–
771 117.

772 De Putter, T., Ruffet, G., Yans, J., & Mees, F. (2015). The age of supergene manganese
773 deposits in Katanga and its implications for the Neogene evolution of the African Great Lakes
774 Region. *Ore Geology Reviews*, *71*, 350–362.

775 Deckart, K., Féraud, G., & Bertrand, H. (1997). Age of Jurassic continental tholeiites of
776 French Guyana, Surinam and Guinea: implications for the initial opening of the Central
777 Atlantic Ocean. *Earth and Planetary Science Letters*, *150*(3–4), 205–220.

778 Deino, A., & Potts, R. (1992). Age-probability spectra for examination of single-crystal
779 40Ar39Ar dating results: Examples from Olorgesailie, southern Kenya Rift. *Quaternary*
780 *International*, *13*, 47–53.

781 Fleck, R. J., Sutter, J. F., & Elliot, D. H. (1977). Interpretation of discordant 40Ar/39Ar
782 age-spectra of Mesozoic tholeiites from Antarctica. *Geochimica et Cosmochimica Acta*, *41*(1),
783 15–32.

784 Gu, P., He, S., Ji, W., Dong, Z., Shi, C., & Chen, F. (2013). Geochemical characteristics
785 of trachyandesite from Dongka Formation, Yushu (Qinghai)： Petrogenesis and its tectonic
786 significance. *Chinese Journal of Geology*, *48*(4), 1069–1082.

787 Guillot, S., & Replumaz, A. (2013). Importance of continental subductions for the growth
788 of the Tibetan plateau. *Bulletin de La Societe Geologique de France*, *184*(3), 199–223.

789 Guillot, S., Goussin, F., Airaghi, L., Replumaz, A., de Sigoyer, J., & Cordier, C. (2019).
790 How and when did the Tibetan Plateau grow? *Russian Geology and Geophysics*, (9).
791 https://doi.org/10.15372/RGG2019126

792 Hacker, B. R., Ratschbacher, L., Webb, L., Ireland, T., Walker, D., & Shuwen, D. (1998).
793 U/Pb zircon ages constrain the architecture of the ultrahigh-pressure Qinling–Dabie Orogen,
794 China. *Earth and Planetary Science Letters*, *161*(1–4), 215–230.

795 Hames, W. E., Cheney, J. T., & Tracy, R. J. (2008). Single-crystal 40Ar/39Ar age
796 variation in muscovite of the Gassetts Schist and associated gneiss, Vermont Appalachians.
797 *American Mineralogist*, *93*(2–3), 384–395.

798 Harris, N. B. W., Ronghua, X., Lewis, C. L., Hawkesworth, C. J., & Yuquan, Z. (1988).
799 Isotope geochemistry of the 1985 Tibet geotraverse, Lhasa to Golmud. *Philosophical*
800 *Transactions of the Royal Society of London. Series A, Mathematical and Physical Sciences*,
801 *327*(1594), 263–285.

802 Hetényi, G., Guillermin, Z., Jordan, M., Raymond, G., Subedi, S., Buchs, N., et al.
803 (2018). Abstract Volume Of The 33Rd Himalaya-Karakorum-Tibet Workshop.

https://doi.org/10.5281/zenodo.1403887

Huang, B., Yan, Y., Piper, J. D. A., Zhang, D., Yi, Z., Yu, S., & Zhou, T. (2018). Paleomagnetic constraints on the paleogeography of the East Asian blocks during Late Paleozoic and Early Mesozoic times. *Earth-Science Reviews*, *186*, 8–36. https://doi.org/10.1016/j.earscirev.2018.02.004

Huang, X., Jing, Z., Xie, F., & Zhao, J. (2019). Late quaternary slip rate of the east segment of the Yushu fault in the central-eastern Tibetan Plateau. *Quaternary International*, *532*, 146–156. https://doi.org/10.1016/j.quaint.2019.11.029

Jackson, S. E., Pearson, N. J., Griffin, W. L., & Belousova, E. A. (2004). The application of laser ablation-inductively coupled plasma-mass spectrometry to in situ U–Pb zircon geochronology. *Chemical Geology*, *211*(1), 47–69. https://doi.org/10.1016/j.chemgeo.2004.06.017

Jian, X., Weislogel, A., & Pullen, A. (2019). Triassic Sedimentary Filling and Closure of the Eastern Paleo-Tethys Ocean: New Insights From Detrital Zircon Geochronology of Songpan-Ganzi, Yidun, and West Qinling Flysch in Eastern Tibet. *Tectonics*, *38*(2), 767–787. https://doi.org/10.1029/2018TC005300

Jin, G. S. (2006). Geochronology and Geochemistry Characters on Some Magmatic Rocks in the West of Xijir Ulan-Jinshajiang Suture Zone (in Chinese with English Abstract). *Chinese Academy of Geological Sciences*, 1–78.

Jolivet, M. (2017). Mesozoic tectonic and topographic evolution of Central Asia and Tibet: a preliminary synthesis. *Geological Society, London, Special Publications*, *427*(1), 19–55. https://doi.org/10.1144/SP427.2

Jourdan, F., & Renne, P. R. (2007). Age calibration of the Fish Canyon sanidine 40Ar/39Ar dating standard using primary K–Ar standards. *Geochimica et Cosmochimica Acta*, *71*(2), 387–402.

Jourdan, F., Verati, C., & Féraud, G. (2006). Intercalibration of the Hb3gr 40Ar/39Ar dating standard. *Chemical Geology*, *231*(3), 177–189.

Kapp, P., Yin, A., Manning, C. E., Murphy, M., Harrison, T. M., Spurlin, M., et al. (2000). Blueschist-bearing metamorphic core complexes in the Qiangtang block reveal deep crustal structure of northern Tibet. *Geology*, *28*(1), 19–22.

Kapp, P., Yin, A., Manning, C. E., Harrison, T. M., Taylor, M. H., & Ding, L. (2003). Tectonic evolution of the early Mesozoic blueschist-bearing Qiangtang metamorphic belt, central Tibet. *Tectonics*, *22*(4), 1043. https://doi.org/10.1029/2002TC001383

Konstantinovskaia, E. A., Brunel, M., & Malavieille, J. (2003). Discovery of the Paleo-Tethys residual peridotites along the Anyemaqen–KunLun suture zone (North Tibet). *Comptes Rendus Geoscience*, *335*(8), 709–719.

Li, G.-M., Li, J.-X., Zhao, J.-X., Qin, K.-Z., Cao, M.-J., & Evans, N. J. (2015). Petrogenesis and tectonic setting of Triassic granitoids in the Qiangtang terrane, central Tibet: Evidence from U–Pb ages, petrochemistry and Sr–Nd–Hf isotopes. *Journal of Asian Earth Sciences*, *105*, 443–455. https://doi.org/10.1016/j.jseaes.2015.02.017

Li, J., Chen, W., Yong, Y., Chen, Y.-L., Sun, J.-B., Zhang, Y., et al. (2012). Emplacement age, geochemical characteristics and tectonic significance of Zhaxike quartz diorite in Yushu area, Qinghai province. *Diqiu Xuebao (Acta Geoscientica Sinica)*, *33*(5), 773–786.

Li, L., Fan, M., Davila, N., Jesmok, G., Mitsunaga, B., Tripati, A., & Orme, D. (2018). Carbonate stable and clumped isotopic evidence for late Eocene moderate to high elevation of the east-central Tibetan Plateau and its geodynamic implications. *GSA Bulletin*. https://doi.org/10.1130/B32060.1

Li, S., Kusky, T. M., Wang, L., Zhang, G., Lai, S., Liu, X., et al. (2007). Collision leading to multiple-stage large-scale extrusion in the Qinling orogen: Insights from the Mianlue suture. *Gondwana Research*, *12*(1), 121–143. https://doi.org/10.1016/j.gr.2006.11.011

Liu, B., Ma, C.-Q., Guo, P., Sun, Y., Gao, K., & Guo, Y.-H. (2016). Evaluation of late Permian mafic magmatism in the central Tibetan Plateau as a response to plume-subduction interaction. *Lithos*, *264*, 1–16. https://doi.org/10.1016/j.lithos.2016.08.011

Liu, B., Ma, C.-Q., Guo, Y.-H., Xiong, F.-H., Guo, P., & Zhang, X. (2016). Petrogenesis and tectonic implications of Triassic mafic complexes with MORB/OIB affinities from the western Garzê-Litang ophiolitic mélange, central Tibetan Plateau. *Lithos*, *260*, 253–267. https://doi.org/10.1016/j.lithos.2016.06.009

Liu, Yan, Tan, J., Wei, J., Zhao, S., Liu, X., Gan, J., & Wang, Z. (2019). Sources and petrogenesis of Late Triassic Zhiduo volcanics in the northeast Tibet: Implications for tectonic evolution of the western Jinsha Paleo-Tethys Ocean. *Lithos*, *336–337*, 169–182. https://doi.org/10.1016/j.lithos.2019.04.005

Liu, Yin, Li, R., Ji, W., Pan, S., Shi, C., Chen, F., et al. (2010). The definition and geological significance of Permian-Triassic magmatic arc at Dangjiangrong, south of Duocai ophiolite mélange zone in the Zhiduo area, Qinhai, China [in Chinese with English abstract]. *Geological Bulletin of China*, *29*(12), 1840–1850.

Liu, Yin, Li, R. S., Ji, W. H., Pan, S. J., Chen, F. N., & Zhang, H. D. (2014). The pairing relationship between ophiolite and arc volcanic rocks along western Jinsha River suture zone and its geological significance: Evidence from geochemistry and LA-ICP-MS zircon U-Pb dating (in Chinese with English Abstract). *Geological Bulletin of China*, *33*(7), 1076–1088.

Liu, Yin, Xiao, W., Windley, B. F., Li, R., Ji, W., Zhou, K., et al. (2019). Late Triassic ridge subduction of Paleotethys: Insights from high-Mg granitoids in the Songpan-Ganzi area of northern Tibet. *Lithos*, *334–335*, 254–272. https://doi.org/10.1016/j.lithos.2019.03.012

Liu, Yin, Xiao, W., Windley, B. F., Zhou, K., Li, R., Zhan, M., et al. (2021). Three stages of arc migration in the Carboniferous-Triassic in northern Qiangtang, central Tibet, China: Ridge subduction and asynchronous slab rollback of the Jinsha Paleotethys. *GSA Bulletin*, *133*(11–12), 2485–2500. https://doi.org/10.1130/B35906.1

Ma, Y., Wang, Q., Wang, J., Yang, T., Tan, X., Dan, W., et al. (2019). Paleomagnetic Constraints on the Origin and Drift History of the North Qiangtang Terrane in the Late Paleozoic. *Geophysical Research Letters*, *46*(2), 689–697. https://doi.org/10.1029/2018GL080964

Metcalfe, I. (2021). Multiple Tethyan ocean basins and orogenic belts in Asia. *Gondwana Research*, *100*, 87–130. https://doi.org/10.1016/j.gr.2021.01.012

Nosenzo, F., Manzotti, P., Poujol, M., Ballèvre, M., & Langlade, J. (2022). A window into an older orogenic cycle: P–T conditions and timing of the pre-Alpine history of the Dora-Maira Massif (Western Alps). *Journal of Metamorphic Geology*, *40*(4), 789–821. https://doi.org/10.1111/jmg.12646

Paton, C., Woodhead, J. D., Hellstrom, J. C., Hergt, J. M., Greig, A., & Maas, R. (2010). Improved laser ablation U-Pb zircon geochronology through robust downhole fractionation correction. *Geochemistry, Geophysics, Geosystems*, *11*(3).

Paton, C., Hellstrom, J., Paul, B., Woodhead, J., & Hergt, J. (2011). Iolite: Freeware for the visualisation and processing of mass spectrometric data. *Journal of Analytical Atomic Spectrometry*, *26*(12), 2508–2518.

Perrot, M., Tremblay, A., Ruffet, G., Labrousse, L., Gervais, F., & Caroir, F. (2020). Diachronic metamorphic and structural evolution of the Connecticut Valley–Gaspé trough, Northern Appalachians. *Journal of Metamorphic Geology*, *38*(1), 3–27. https://doi.org/10.1111/jmg.12510

Pullen, A., Kapp, P., Gehrels, G. E., Vervoort, J. D., & Ding, L. (2008). Triassic continental subduction in central Tibet and Mediterranean-style closure of the Paleo-Tethys Ocean. *Geology*, *36*(5), 351–354. https://doi.org/10.1130/G24435A.1

Pullen, A., Kapp, P., Gehrels, G. E., Ding, L., & Zhang, Q. (2011). Metamorphic rocks in central Tibet: Lateral variations and implications for crustal structure. *Geological Society of America Bulletin*, *123*(3–4), 585–600.

Reid, A., Wilson, C. J. L., & Liu, S. (2005). Structural evidence for the Permo-Triassic tectonic evolution of the Yidun Arc, eastern Tibetan Plateau. *Journal of Structural Geology*, *27*(1), 119–137. https://doi.org/10.1016/j.jsg.2004.06.011

Reid, A., Wilson, C. J. L., Shun, L., Pearson, N., & Belousova, E. (2007). Mesozoic plutons of the Yidun Arc, SW China: U/Pb geochronology and Hf isotopic signature. *Ore Geology Reviews*, *31*(1), 88–106. https://doi.org/10.1016/j.oregeorev.2004.11.003

Renne, P. R., Swisher, C. C., Deino, A. L., Karner, D. B., Owens, T. L., & DePaolo, D. J. (1998). Intercalibration of standards, absolute ages and uncertainties in 40Ar/39Ar dating. *Chemical Geology*, *145*(1–2), 117–152.

Renne, P. R., Mundil, R., Balco, G., Min, K., & Ludwig, K. R. (2010). Joint determination of 40K decay constants and 40Ar∗/40K for the Fish Canyon sanidine standard, and improved accuracy for 40Ar/39Ar geochronology. *Geochimica et Cosmochimica Acta*, *74*(18), 5349–5367.

Renne, P. R., Balco, G., Ludwig, K. R., Mundil, R., & Min, K. (2011). Response to the comment by WH Schwarz et al. on "Joint determination of 40K decay constants and 40Ar∗/40K for the Fish Canyon sanidine standard, and improved accuracy for 40Ar/39Ar geochronology" by PR Renne et al.(2010). *Geochimica et Cosmochimica Acta*, *75*(17), 5097–5100.

Replumaz, A., Funiciello, F., Reitano, R., Faccenna, C., & Balon, M. (2016). Asian collisional subduction: A key process driving formation of the Tibetan Plateau. *Geology*, *44*(11), 943–946. https://doi.org/10.1130/G38276.1

Roddick, J. C. (1983). High precision intercalibration of 40Ar-39Ar standards. *Geochimica et Cosmochimica Acta*, *47*(5), 887–898.

Roger, F., Tapponnier, P., Arnaud, N., Schärer, U., Brunel, M., Zhiqin, X., & Jingsui, Y. (2000). An Eocene magmatic belt across central Tibet: mantle subduction triggered by the Indian collision? *Terra Nova*, *12*(3), 102–108. https://doi.org/10.1046/j.1365-3121.2000.123282.x

Roger, F., Arnaud, N., Gilder, S., Tapponnier, P., Jolivet, M., Brunel, M., et al. (2003). Geochronological and geochemical constraints on Mesozoic suturing in east central Tibet: CHRONOLOGY OF MESOZOIC SUTURES IN TIBET. *Tectonics*, *22*(4), n/a-n/a. https://doi.org/10.1029/2002TC001466

Roger, F., Jolivet, M., & Malavieille, J. (2008). Tectonic evolution of the Triassic fold belts of Tibet. *Comptes Rendus Geoscience*, *340*(2–3), 180–189. https://doi.org/10.1016/j.crte.2007.10.014

Roger, F., Jolivet, M., & Malavieille, J. (2010). The tectonic evolution of the Songpan-Garzê (North Tibet) and adjacent areas from Proterozoic to Present: A synthesis. *Journal of Asian Earth Sciences*, *39*(4), 254–269. https://doi.org/10.1016/j.jseaes.2010.03.008

Rohrmann, A., Kapp, P., Carrapa, B., Reiners, P. W., Guynn, J., Ding, L., & Heizler, M. (2012). Thermochronologic evidence for plateau formation in central Tibet by 45 Ma.

Rowley, D. B., Xue, F., Tucker, R. D., Peng, Z. X., Baker, J., & Davis, A. (1997). Ages of ultrahigh pressure metamorphism and protolith orthogneisses from the eastern Dabie Shan: U/Pb zircon geochronology. *Earth and Planetary Science Letters*, *151*(3), 191–203. https://doi.org/10.1016/S0012-821X(97)81848-1

Ruffet, G., Féraud, G., & Amouric, M. (1991). Comparison of 40Ar-39Ar conventional and laser dating of biotites from the North Trégor Batholith. *Geochimica et Cosmochimica Acta*, *55*(6), 1675–1688. https://doi.org/10.1016/0016-7037(91)90138-U

Ruffet, G., Féraud, G., Balèvre, M., & Kiénast, J.-R. (1995). Plateau ages and excess argon in phengites: an 40Ar-39Ar laser probe study of Alpine micas (Sesia Zone, Western Alps, northern Italy). *Chemical Geology*, *121*(1), 327–343. https://doi.org/10.1016/0009-2541(94)00132-R

Shangyou, N., Rowley, D. B., & Ziegler, A. M. (1990). Constraints on the locations of Asian microcontinents in Palaeo-Tethys during the Late Palaeozoic. *Geological Society, London, Memoirs*, *12*(1), 397–409.

de Sigoyer, J., Vanderhaeghe, O., Duchêne, S., & Billerot, A. (2014). Generation and emplacement of Triassic granitoids within the Songpan Ganze accretionary-orogenic wedge in a context of slab retreat accommodated by tear faulting, Eastern Tibetan plateau, China. *Journal of Asian Earth Sciences*, *88*, 192–216. https://doi.org/10.1016/j.jseaes.2014.01.010

Sláma, J., Košler, J., Condon, D. J., Crowley, J. L., Gerdes, A., Hanchar, J. M., et al.

(2008). Plešovice zircon—a new natural reference material for U–Pb and Hf isotopic microanalysis. *Chemical Geology*, *249*(1–2), 1–35. https://doi.org/10.1016/j.chemgeo.2007.11.005

Song, P., Ding, L., Li, Z., Lippert, P. C., & Yue, Y. (2017). An early bird from Gondwana: Paleomagnetism of Lower Permian lavas from northern Qiangtang (Tibet) and the geography of the Paleo-Tethys. *Earth and Planetary Science Letters*, *475*, 119–133. https://doi.org/10.1016/j.epsl.2017.07.023

Spurlin, M. S., Yin, A., Horton, B. K., Zhou, J., & Wang, J. (2005). Structural evolution of the Yushu-Nangqian region and its relationship to syncollisional igneous activity, east-central Tibet. *Geological Society of America Bulletin*, *117*(9–10), 1293–1317.

Staisch, L. M., Niemi, N. A., Clark, M. K., & Chang, H. (2016). Eocene to late Oligocene history of crustal shortening within the Hoh Xil Basin and implications for the uplift history of the northern Tibetan Plateau. *Tectonics*, *35*(4), 862–895. https://doi.org/10.1002/2015TC003972

Tan, J., Wei, J.-H., Zhao, X.-F., Zhao, S.-Q., Liu, Y., Zhang, F., & Liu, X.-Y. (2020). Late paleozoic to early mesozoic paleo-tethys tectonic evolution of central NE Tibetan Plateau: Insights from the Zhiduo mafic-ultramafic complex. *Lithos*, *364–365*, 105534. https://doi.org/10.1016/j.lithos.2020.105534

Tapponnier, P., Zhiqin, X., Roger, F., Meyer, B., Arnaud, N., Wittlinger, G., & Jingsui, Y. (2001). Oblique stepwise rise and growth of the Tibet Plateau. *Science*, *294*(5547), 1671–1677.

Tartese, R., Ruffet, G., Poujol, M., Boulvais, P., & Ireland, T. R. (2011). Simultaneous resetting of the muscovite K-Ar and monazite U-Pb geochronometers: a story of fluids. *Terra Nova*, *23*(6), 390–398.

Tremblay, A., Ruffet, G., & Bédard, J. H. (2011). Obduction of Tethyan-type ophiolites—A case-study from the Thetford-Mines ophiolitic Complex, Quebec Appalachians, Canada. *Lithos*, *125*(1–2), 10–26.

Tremblay, A., Ruffet, G., & Lemarchand, J. (2020). Timing and duration of Archean orogenic gold deposits in the Bourlamaque pluton, Val d'Or mining camp, Abitibi, Canada. *Ore Geology Reviews*, *127*, 103812.

Turner, G. (1968). The distribution of potassium and argon in chondrites. In *Origin and Distribution of the Elements* (pp. 387–398). Elsevier.

Turner, G. (1971). 40Ar39Ar ages from the lunar maria. *Earth and Planetary Science Letters*, *11*(1–5), 169–191.

Vermeesch, P. (2018). IsoplotR: A free and open toolbox for geochronology. *Geoscience Frontiers*, *9*(5), 1479–1493. https://doi.org/10.1016/j.gsf.2018.04.001

Wang, B. Z., Luo, Z. H., Zeng, X. P., Wang, Y. Z., & Qi, S. S. (2008). Indosinian granitoids in the Zhiduo area in the northern segment of the Sanjiang belt, Qinghai: their petrogenesis and zircon U–Pb dating (in Chinese with English Abstract). *Geol. China*, *35*, 196–206.

Wang, X., Hu, K.-Y., Shi, Y.-K., Chen, J.-T., Yang, S.-R., Ye, X.-Y., et al. (2021). The missing upper Carboniferous in the Cimmerian continent: A critical review. *Earth-Science Reviews*, *217*, 103627.

Yang, T.-N., Zhang, H. R., Liu, Y. X., Wang, Z. L., Song, Y. C., Yang, Z. S., et al. (2011). Permo-Triassic arc magmatism in central Tibet: Evidence from zircon U–Pb geochronology, Hf isotopes, rare earth elements, and bulk geochemistry. *Chemical Geology*, *284*(3–4), 270–282. https://doi.org/10.1016/j.chemgeo.2011.03.006

Yang, T.-N., Hou, Z.-Q., Wang, Y., Zhang, H.-R., & Wang, Z.-L. (2012). Late Paleozoic to Early Mesozoic tectonic evolution of northeast Tibet: Evidence from the Triassic composite western Jinsha-Garzê-Litang suture: Paleo-Tethyan tectonics of North-East Tibet. *Tectonics*, *31*(4), n/a-n/a. https://doi.org/10.1029/2011TC003044

Yang, T.-N., Ding, Y., Zhang, H. R., Fan, J. W., Liang, M. J., & Wang, X. H. (2014). Two-phase subduction and subsequent collision defines the Paleotethyan tectonics of the southeastern Tibetan Plateau: Evidence from zircon U-Pb dating, geochemistry, and structural geology of the Sanjiang orogenic belt, southwest China. *Geological Society of America Bulletin*, *126*(11–12), 1654–1682. https://doi.org/10.1130/B30921.1

Yin, A., & Harrison, T. M. (2000). Geologic evolution of the Himalayan-Tibetan orogen. *Annual Review of Earth and Planetary Sciences*, *28*(1), 211–280.

Yong, Y., Chen, W., Zhang, Y., & Liu, X. Y. (2011). Zircon SHRIMP U–Pb dating and geochemistry of the Rangnianggongba gabbro in Yushu area, Qinghai Province. *Acta Petrologica et Mineralogica*, *30*(3), 419–426.

Zanchi, A., Zanchetta, S., Balini, M., & Ghassemi, M. R. (2016). Oblique convergence during the Cimmerian collision: Evidence from the Triassic Aghdarband Basin, NE Iran. *Gondwana Research*, *38*, 149–170. https://doi.org/10.1016/j.gr.2015.11.008

Zhai, Q., Jahn, B., Wang, J., Hu, P., Chung, S., Lee, H., et al. (2016). Oldest Paleo-Tethyan ophiolitic melange in the Tibetan Plateau. *Geological Society of America Bulletin*, *128*(3–4), 355–373. https://doi.org/10.1130/B31296.1

Zhai, Q.-G., Zhang, R.-Y., Jahn, B.-M., Li, C., Song, S.-G., & Wang, J. (2011). Triassic eclogites from central Qiangtang, northern Tibet, China: Petrology, geochronology and metamorphic P–T path. *Lithos*, *125*(1), 173–189. https://doi.org/10.1016/j.lithos.2011.02.004

Zhang, H., Yang, T., Hou, Z., Dai, M., & Hou, K. (2017). Permian back-arc basin basalts in the Yushu area: New constrain on the Paleo-Tethyan evolution of the north-central Tibet. *Lithos*, *286–287*, 216–226. https://doi.org/10.1016/j.lithos.2017.06.012

Zhang, K.-J., Li, B., & Wei, Q.-G. (2012). Diversified Provenance of the Songpan-Ganzi Triassic Turbidites, Central China: Constraints from Geochemistry and Nd Isotopes. *The Journal of Geology*, *120*(1), 69–82. https://doi.org/10.1086/662716

Zhang, Y., Huang, W., Zhang, Y., Poujol, M., Guillot, S., Roperch, P., et al. (2019). Detrital zircon provenance comparison between the Paleocene-Eocene Nangqian-Xialaxiu and Gongjue basins: New insights for Cenozoic paleogeographic evolution of the eastern Tibetan Plateau. *Palaeogeography, Palaeoclimatology, Palaeoecology*, *533*, 109241. https://doi.org/10.1016/j.palaeo.2019.109241

Zhang, Y.-X., Jin, X., Zhang, K.-J., Sun, W.-D., Liu, J.-M., Zhou, X.-Y., & Yan, L.-L. (2018). Newly discovered Late Triassic Baqing eclogite in central Tibet indicates an anticlockwise West–East Qiangtang collision. *Scientific Reports*, *8*(1). https://doi.org/10.1038/s41598-018-19342-w

Zhao, S.-Q., Tan, J., Wei, J.-H., Tian, N., Zhang, D.-H., Liang, S.-N., & Chen, J.-J. (2015). Late Triassic Batang Group arc volcanic rocks in the northeastern margin of Qiangtang terrane, northern Tibet: partial melting of juvenile crust and implications for Paleo-Tethys ocean subduction. *International Journal of Earth Sciences*, *104*(2), 369–387. https://doi.org/10.1007/s00531-014-1080-z

Zhao, S.-Q., Fu, L. B., Wei, J. H., Tan, J., Wang, X. C., Zhao, Z. X., & Li, X. (2015). Petrogenesis and Geodynamic Setting of Late Triassic Quartz Diorites in Zhiduo Area, Qinghai Province. *Earth Science*, *40*(1), 61–76.

Figure.

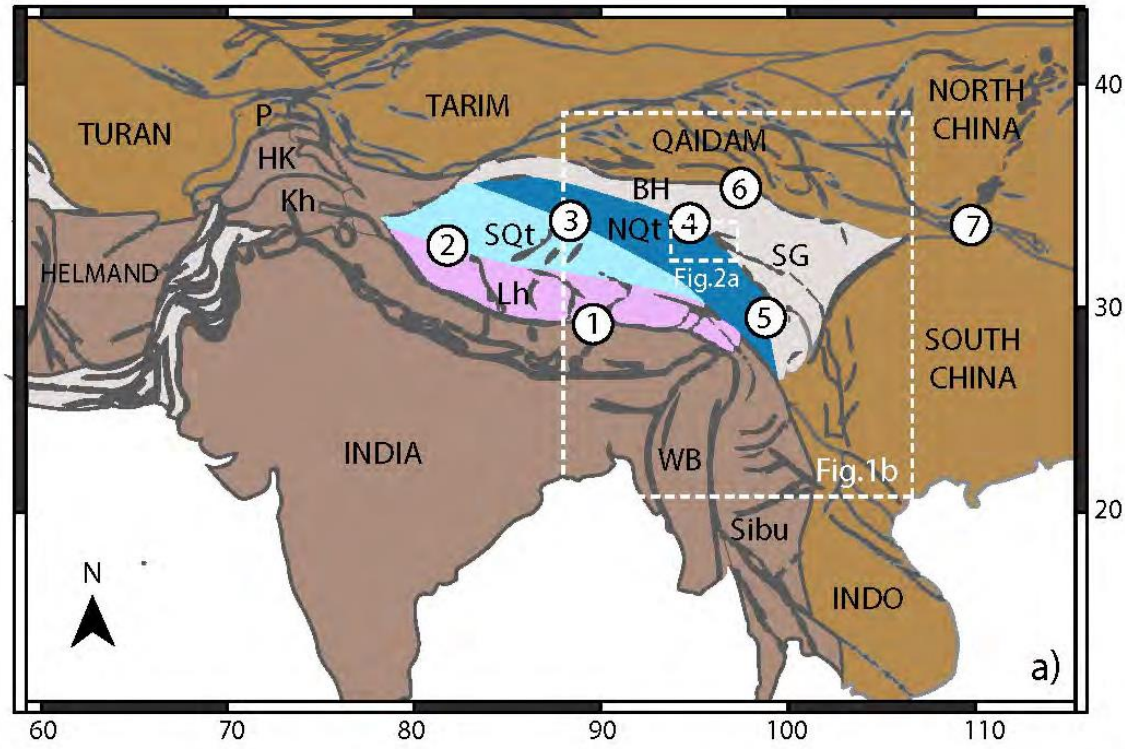
TURAN
P
HK
Kh
TARIM
QAIDAM
NORTH CHINA
BH
NQt
SQt
Lh
SG
HELMAND
Fig.2a
Fig.1b
SOUTH CHINA
INDIA
WB
Sibu
INDO
N
a)
40
30
20
60
70
80
90
100
110

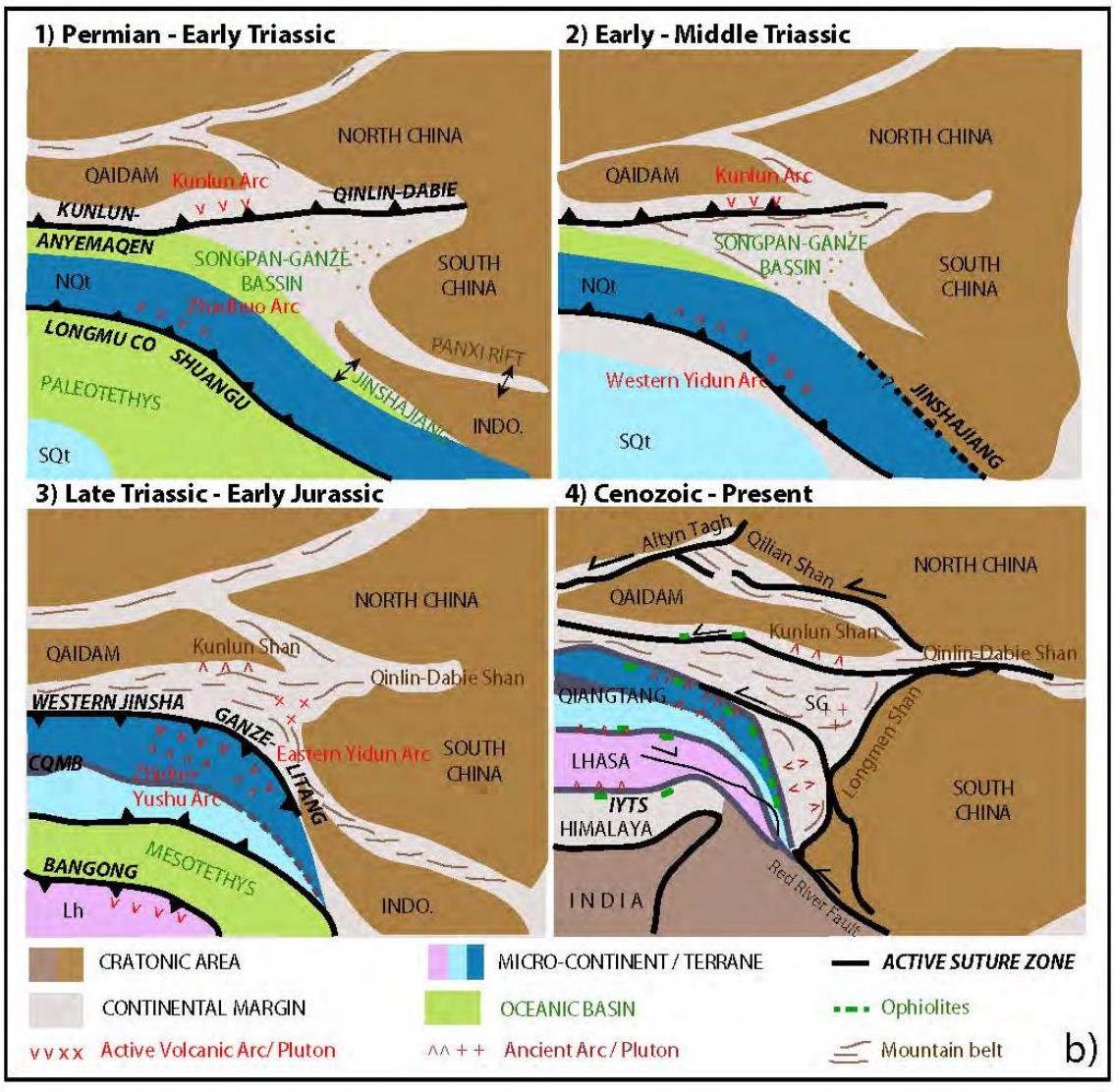
1) Permian - Early Triassic
NORTH CHINA
QAIDAM
Kunlun Arc
QINLIN-DABIE
KUNLUN-
ANYEMAQEN
SONGPAN-GANZE
BASSIN
SOUTH CHINA
NQt
Zhanhuo Arc
LONGMU CO
SHUANGU
PANXI RIFT
JINSHAJIANG
PALEOTETHYS
INDO.
SQt
2) Early - Middle Triassic
NORTH CHINA
QAIDAM
Kunlun Arc
SONGPAN-GANZE
BASSIN
SOUTH CHINA
NQt
Western Yidun Arc
JINSHAJIANG
SQt
3) Late Triassic - Early Jurassic
NORTH CHINA
QAIDAM
Kunlun Shan
Qinlin-Dabie Shan
WESTERN JINSHA
GANZE-
LITANG
Eastern Yidun Arc
SOUTH CHINA
CQMB
Zhiduo
Yushu Arc
BANGONG
MESOTETHYS
Lh
INDO.
4) Cenozoic - Present
Altyn Tagh
Qilian Shan
NORTH CHINA
QAIDAM
Kunlun Shan
Qinlin-Dabie Shan
QIANGTANG
SG
Longmen Shan
LHASA
IYTS
HIMALAYA
SOUTH CHINA
INDIA
Red River Fault
CRATONIC AREA
MICRO-CONTINENT / TERRANE
ACTIVE SUTURE ZONE
CONTINENTAL MARGIN
OCEANIC BASIN
Ophiolites
v v x x Active Volcanic Arc/ Pluton
^^ + + Ancient Arc / Pluton
Mountain belt
b)

Figure 1. a) General map of Southern Asia showing the main continental terranes and the associated suture zones discussed in text (1-10). Two inserts indicate the locations of Figures 1b and 2a. Suture zones: 1, Indus-Yarlung-Zangbo; 2, Bangong Nujiang; 3, Longmu Co-Shanghu; 4, Western Jinsha; 5, Ganze-Litang; 6, Kunlun–Anyemaqen Suture; 7, Qinlin-Dabie. **b)** Summary of the Paleozoic-Mesozoic episodes of Tibetan continental accretion. Modified from Roger et al. (2010) and Yang et al. (2014). Abbreviations: BH, Bayan Har; CQMB, Central Qiangtang Metamorphic Belt; HK, Hindu Kush; INDO, Indochina; Kh, Kohistan; Lh, Lhasa; NQt, North Qiangtang; P, Pamir; SG, Songpan-Ganze; Sibu, Sibumasu; SQt, South Qiangtang; WB, West Burma.

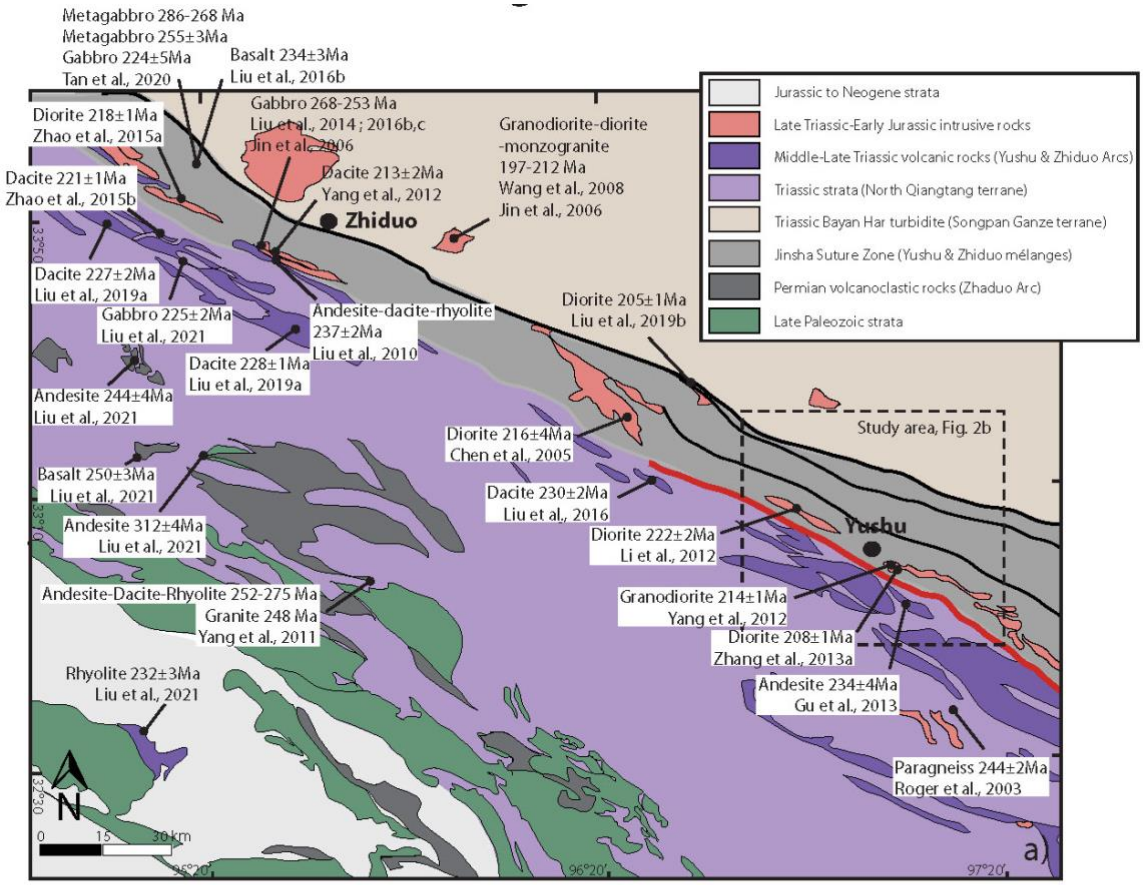
Metagabbro 286-268 Ma
Metagabbro 255±3Ma
Gabbro 224±5Ma
Tan et al., 2020
Basalt 234±3Ma
Liu et al., 2016b
Diorite 218±1Ma
Zhao et al., 2015a
Gabbro 268-253 Ma
Liu et al., 2014 ; 2016b,c
Jin et al., 2006
Granodiorite-diorite
-monzogranite
197-212 Ma
Wang et al., 2008
Jin et al., 2006
Dacite 221±1Ma
Zhao et al., 2015b
Dacite 213±2Ma
Yang et al., 2012
Zhiduo
Dacite 227±2Ma
Liu et al., 2019a
Gabbro 225±2Ma
Liu et al., 2021
Andesite-dacite-rhyolite
237±2Ma
Liu et al., 2010
Diorite 205±1Ma
Liu et al., 2019b
Dacite 228±1Ma
Liu et al., 2019a
Andesite 244±4Ma
Liu et al., 2021
Diorite 216±4Ma
Chen et al., 2005
Study area, Fig. 2b
Basalt 250±3Ma
Liu et al., 2021
Dacite 230±2Ma
Liu et al., 2016
Andesite 312±4Ma
Liu et al., 2021
Diorite 222±2Ma
Li et al., 2012
Yushu
Andesite-Dacite-Rhyolite 252-275 Ma
Granite 248 Ma
Yang et al., 2011
Granodiorite 214±1Ma
Yang et al., 2012
Diorite 208±1Ma
Zhang et al., 2013a
Rhyolite 232±3Ma
Liu et al., 2021
Andesite 234±4Ma
Gu et al., 2013
Paragneiss 244±2Ma
Roger et al., 2003
Jurassic to Neogene strata
Late Triassic-Early Jurassic intrusive rocks
Middle-Late Triassic volcanic rocks (Yushu & Zhiduo Arcs)
Triassic strata (North Qiangtang terrane)
Triassic Bayan Har turbidite (Songpan Ganze terrane)
Jinsha Suture Zone (Yushu & Zhiduo mélanges)
Permian volcanoclastic rocks (Zhaduo Arc)
Late Paleozoic strata
N
0 15 30 km
96°20'
97°20'
a)

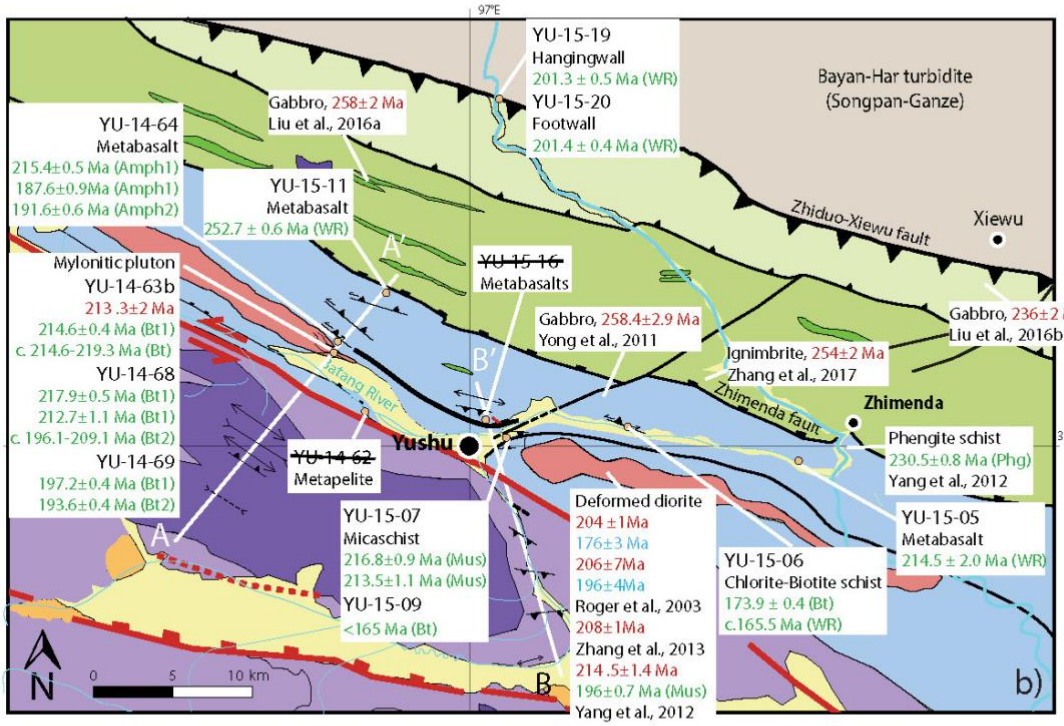
97°E
YU-15-19
Hangingwall
201.3 ± 0.5 Ma (WR)
YU-15-20
Footwall
201.4 ± 0.4 Ma (WR)
Bayan-Har turbidite
(Songpan-Ganze)
Gabbro, 258±2 Ma
Liu et al., 2016a
YU-14-64
Metabasalt
215.4±0.5 Ma (Amph1)
187.6±0.9Ma (Amph1)
191.6±0.6 Ma (Amph2)
YU-15-11
Metabasalt
252.7 ± 0.6 Ma (WR)
Zhiduo-Xiewu fault
Xiewu
A'
YU-15-16
Metabasalts
Mylonitic pluton
YU-14-63b
213 .3±2 Ma
214.6±0.4 Ma (Bt1)
c. 214.6-219.3 Ma (Bt)
Gabbro, 258.4±2.9 Ma
Yong et al., 2011
Gabbro, 236±2 Ma
Liu et al., 2016b
Ignimbrite, 254±2 Ma
Zhang et al., 2017
B'
Jatang River
Zhimenda fault
Zhimenda
YU-14-68
217.9±0.5 Ma (Bt1)
212.7±1.1 Ma (Bt1)
c. 196.1-209.1 Ma (Bt2)
YU-14-69
197.2±0.4 Ma (Bt1)
193.6±0.4 Ma (Bt2)
Yushu
YU-14-62
Metapelite
Phengite schist
230.5±0.8 Ma (Phg)
Yang et al., 2012
33°N
Deformed diorite
204 ±1Ma
176±3 Ma
206±7Ma
196±4Ma
Roger et al., 2003
208±1Ma
Zhang et al., 2013
214 .5±1.4 Ma
196±0.7 Ma (Mus)
Yang et al., 2012
YU-15-07
Micaschist
216.8±0.9 Ma (Mus)
213.5±1.1 Ma (Mus)
YU-15-09
<165 Ma (Bt)
YU-15-06
Chlorite-Biotite schist
173.9 ± 0.4 (Bt)
c.165.5 Ma (WR)
YU-15-05
Metabasalt
214.5 ± 2.0 Ma (WR)
A
B
N
0 5 10 km
b)
Songpang-Ganze terrane
Bayan Har Triassic flysch
Qiangtang terrane
Quaternary deposits
Cenozoic strata
Upper Triassic strata
Upper Triassic Yushu Arc volcanics/plutons
Yushu mélange
Upper stratigraphic units
- conglomerate, sandstone, limestone, dark grey slate, chlorite schist + ultramafic rocks
Lower «Tectonostratigraphic» unit
- blueschist to greenschist facies alternations of metabasalt, marble, phyllite, metagreywacke
Ultramafic lenses
Fold axis trace
Left-lateral fault
Inferred fault
Thrust
Normal fault
River
Active Yushu Fault (after Chevalier et al., 2018)
Dating methods:
204 ±1Ma U-Pb on zircon
176±3 Ma Rb-Sr on feldspar and/or whole-rock
Ar-Ar on (mineral)
217.9±0.5 Ma (Bt1) Plateau age
212.7±1.1 Ma (Bt1) Pseudo-plateau age
c. 196.1-209.1 Ma (Bt2) Apparent ages
Sampling sites

Figure 2. a) Geological map of the Yushu-Zhiduo area in northeastern Qiangtang, showing the distribution of recently dated Mesozoic magmatic rocks along the Western Jinsha Suture. Modified from Liu et al. (2021) and Yang et al. (2014). The location of our study area is indicated by the insert. **b)** Map of the Yushu mélange and adjacent areas, modified from Yang et al. (2012), Zhang et al. (2017) and the Geological Survey of Qinghai Province 1:250 000 Geological Map (2005), according to our observations. Available age data for magmatic and deformed rocks are reported. AA' and BB' indicate respectively the western and eastern cross-sections of Figure 3a,b.

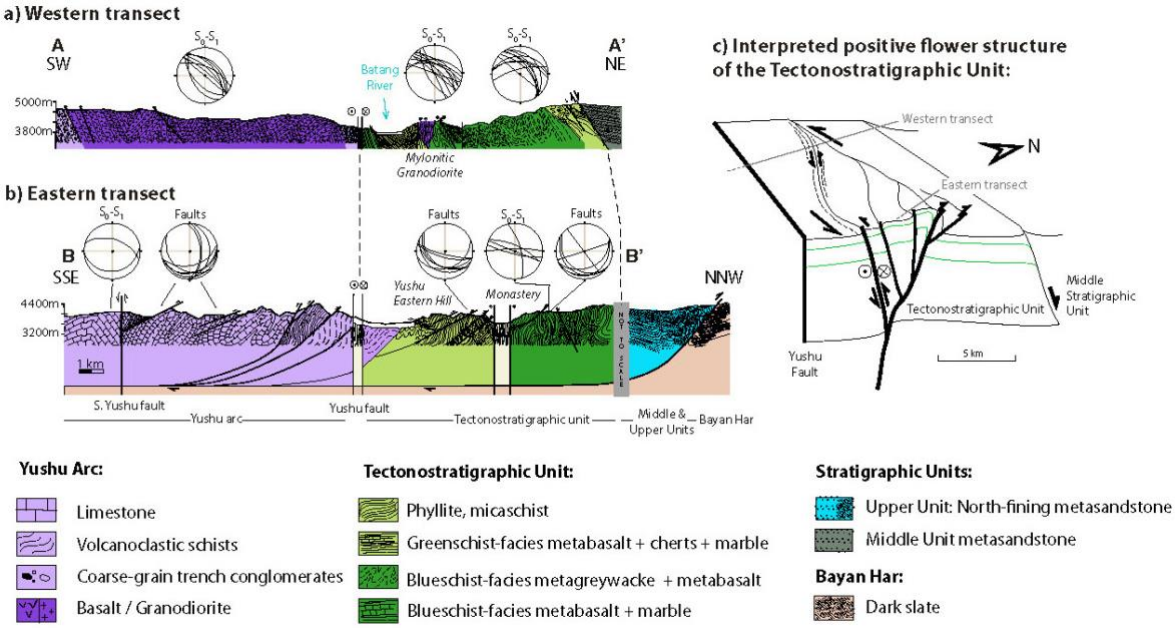

Figure 3. a-b) Structural cross-sections of the Yushu mélange, with stereographic projections (lower hemisphere, equal area net) of the observed fabrics. **c)** Schematic interpretation of the structures of the *Tectonostratigraphic* unit as part of a large-scale positive flower structure, resulting from regional transpressive deformation (see the text for explanation).

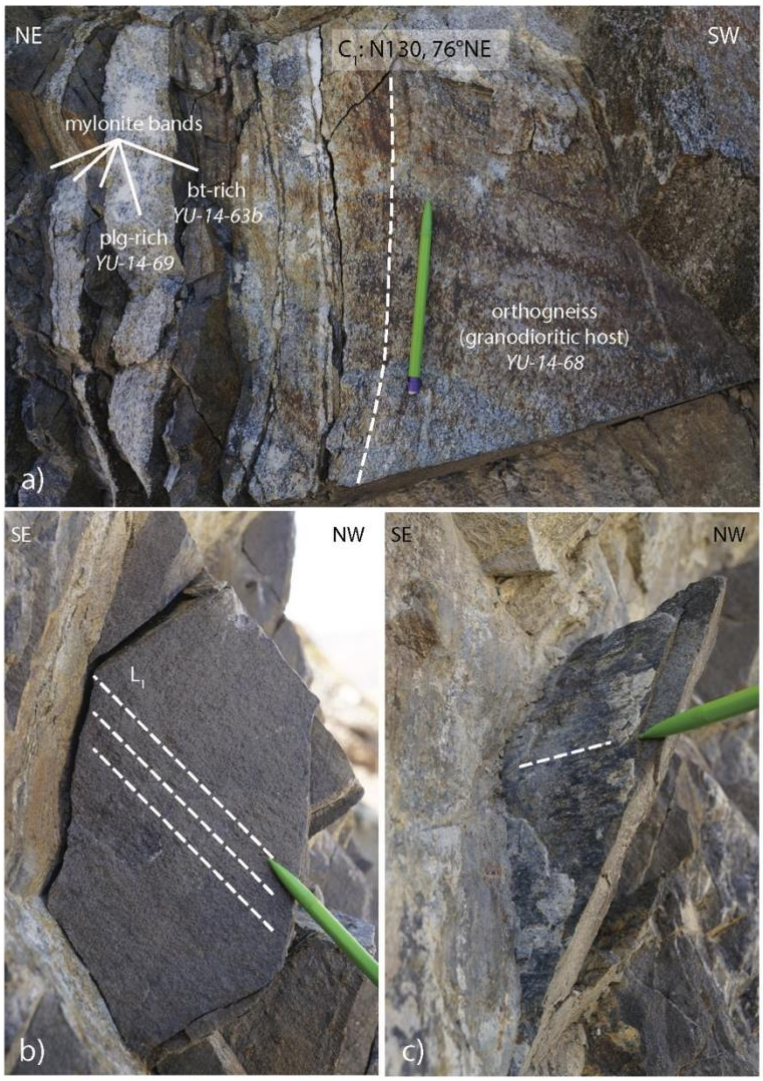

Figure 4. Outcrop pictures of the mylonitic granodiorite pluton (western transect). **a)** Heterogeneous composition of the pluton, with mylonite bands wrapping a much less deformed granodiorite lens. The main C_1 shear planes direction is indicated. **b)** Surface of a C_1 plane within a mylonitic band, showing L_1 lineation defined by the alignment of tiny biotite flakes. **c)** Late sub-horizontal brittle striation on a slickenside, corresponding to a C_1 plane, and related to the present-day activity of the Yushu fault.

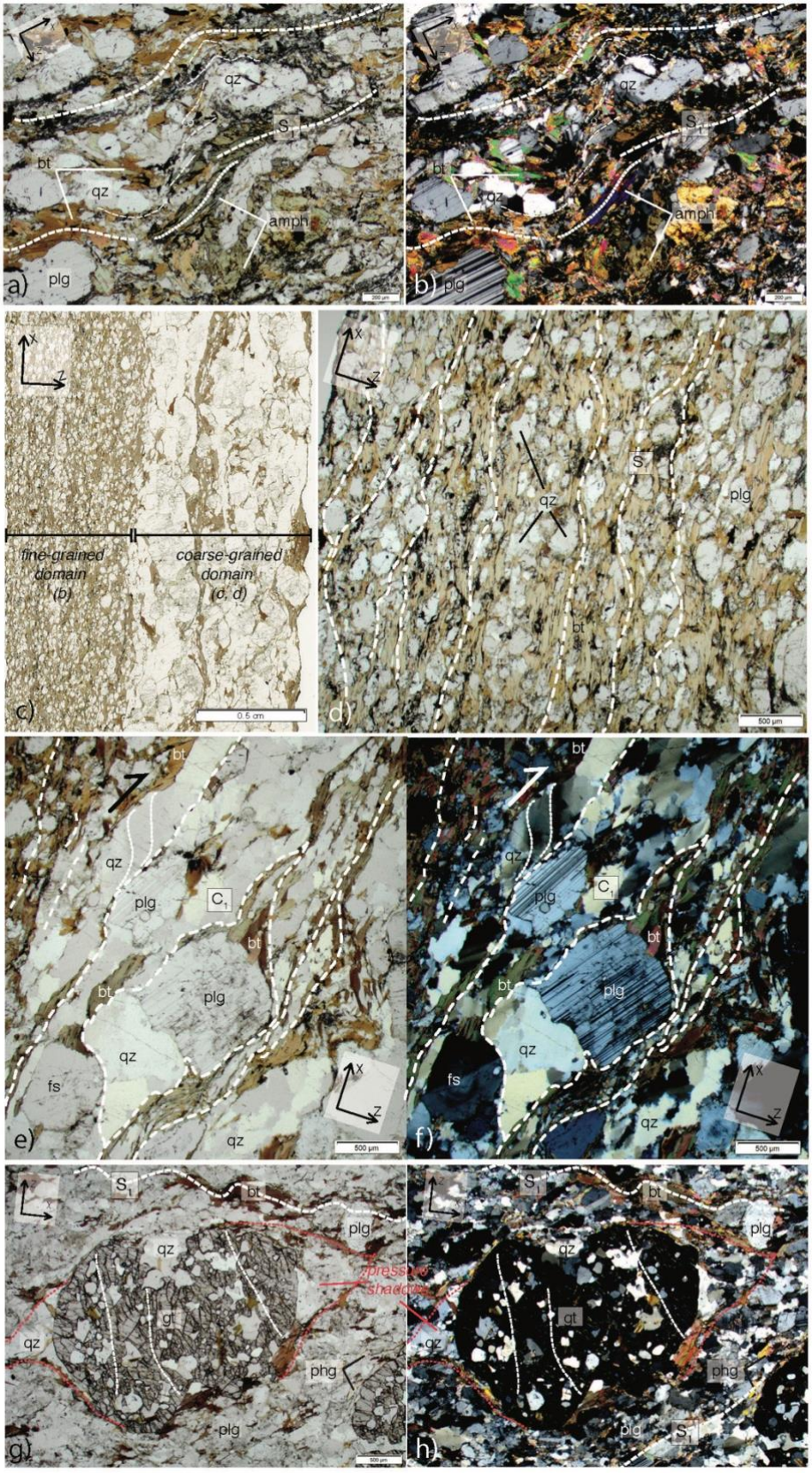

Figure 5. Interpreted optical microphotographs of samples from the mylonitic granodiorite pluton. S_1 foliation is underlined by white dashed lines; stretching direction (X)

is N130. **a-b)** Least deformed part of the granodiorite pluton (sample YU-14-68), using parallel light and crossed Nicols. **c)** Thin-section scan showing the contact between a fine-grained mylonitic band (left) and a coarse-grained orthogneiss domain (right). **d)** Fine-grained mylonitic band (sample YU-14-63b), using parallel light. **e-f)** Coarse-grained domain, using parallel light and crossed Nicols; the internal deformation of quartz grains is underlined. **g-h)** Garnet-bearing, quartz-rich mylonite band (sample YU-14-69), using parallel light and crossed Nicols; red dotted lines delineate pressure shadows. Mineral abbreviations: amph, amphibole; bt, biotite; fs, alkali feldspar; gt, garnet; plg, plagioclase; qz, quartz.

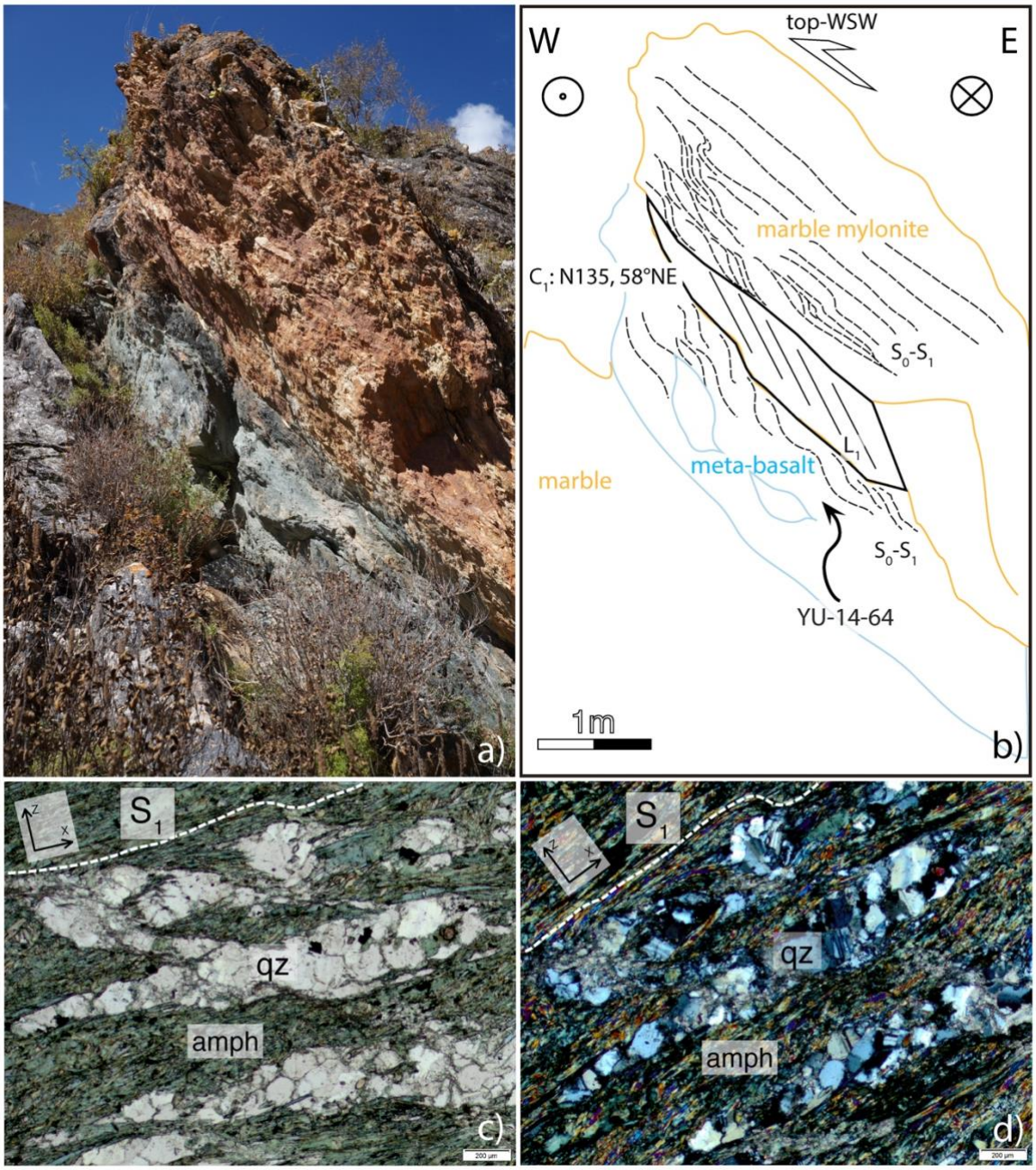

Figure 6. a) Field picture and **b)** structural interpretation of a top-to-the-WSW transpressive shear contact between marble and blueschists with metabasalt lenses (sampling site of YU-14-64). **c-d)** Interpreted microphotographs of the metabasaltic sample YU-14-64 using parallel light (c) and crossed Nicols (d). The main foliation plane S_1 is underlined with a white dashed line. Mineral abbreviations: amph, amphibole; qz, quartz, plg, plagioclase.

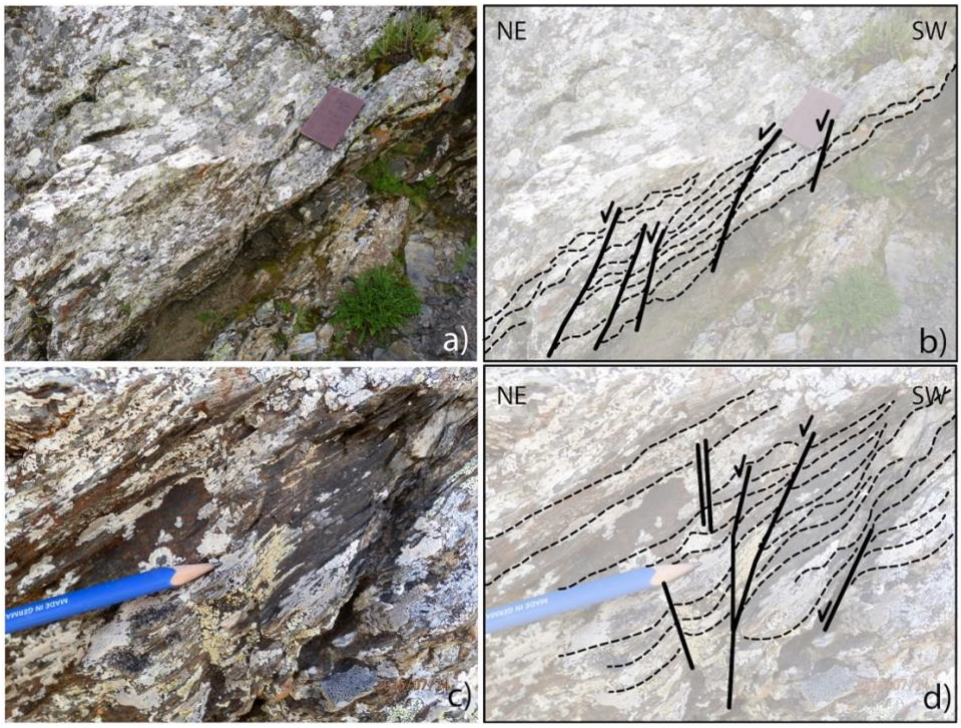

Figure 7. Field pictures (a,c) and structural interpretations (b,d) of top-to-the-NE normal shear within the hanging wall of the Zhimenda fault (sampling site of YU-15-11). Dashed lines indicate the main foliation planes, thick lines indicate shear planes.

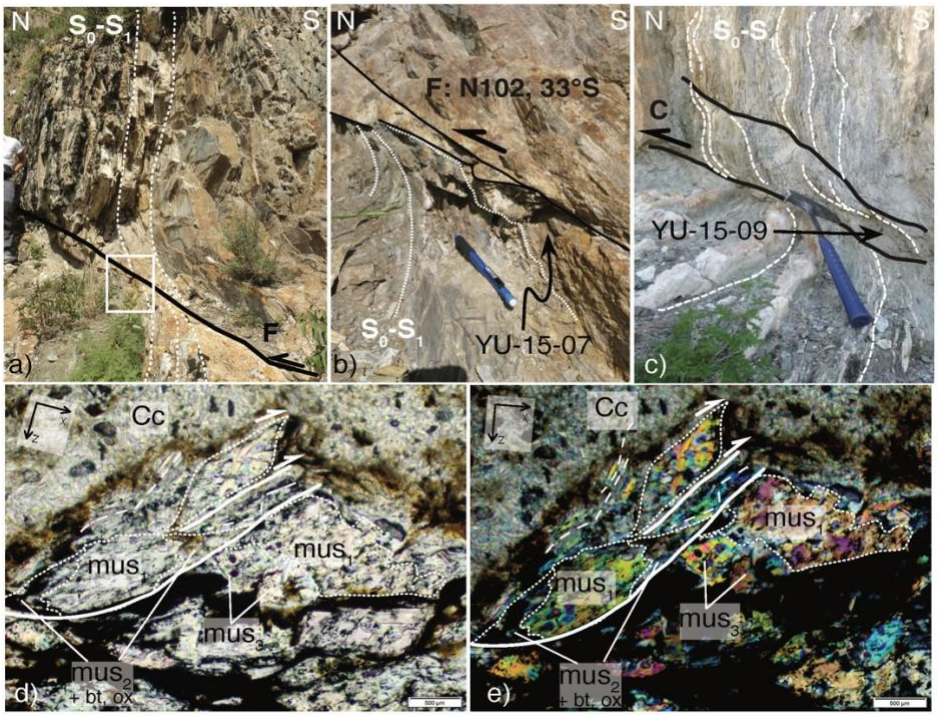

Figure 8. Top-to-the-north brittle structures affecting the subvertical S_0/S_1 schistosity on the eastern hill of the Yushu city. **a,b)** Interpreted field picture of a fault plane on muscovite-bearing schists (sampling site of YU-15-07). **c)** Interpreted field picture of a shear plane in cherts with quartz-chlorite and calcite veins (sampling site of YU-15-09). **d-e)** Interpreted microphotographs of the fault plane sample YU-14-07, using parallel light (d) and crossed Nicols (e). White dashed lines underline the foliation planes; solid white lines indicate glide planes or micro-thrusts between grains; white dotted lines delineate muscovite grain boundaries. mus_1 are deformed porphyroclasts, mus_2 and mus_3 are syn-deformation (re)crystallized grains. Mineral abbreviations: Cc, carbonate; bt, biotite; ox, oxide; mus, muscovite; qz, quartz.

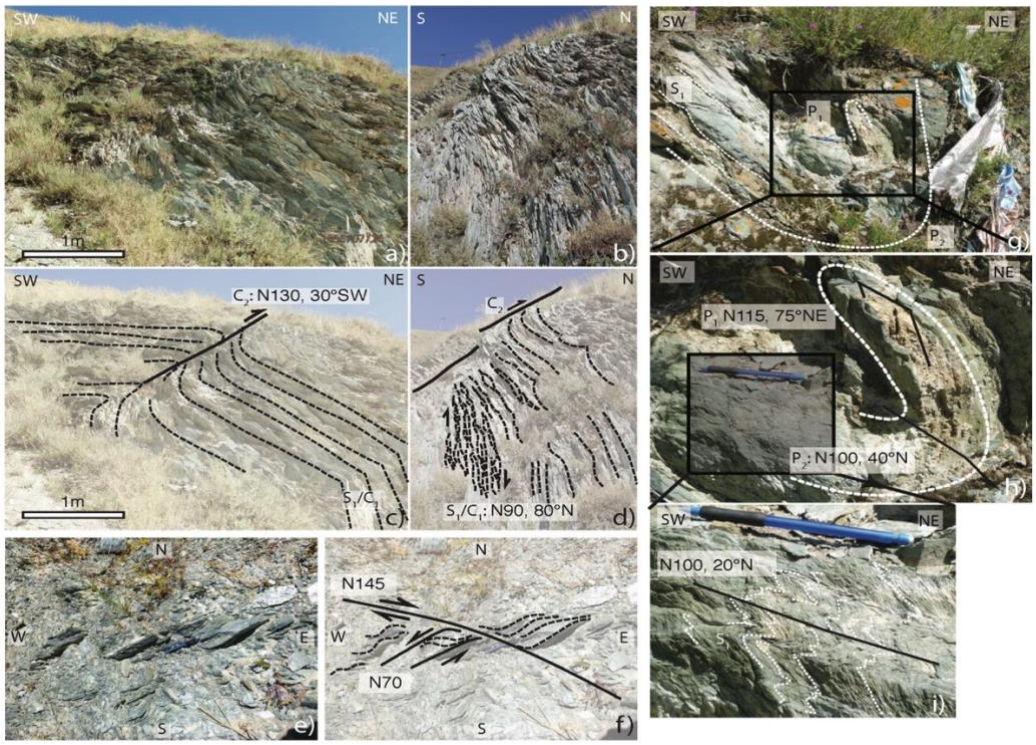

Figure 9. Ductile structures affecting blueschist-facies metabasalts on the Yushu monastery hill, north of the city (sampling sites of YU-15-16 and YU-15-17). **a,b)** Field pictures and **c,d)** structural interpretation: the main apparent subvertical foliation S_1 presents shear structures, suggesting that the foliation was transposed during a first deformation phase. This S_1/C_1 planes are affected by top-to-the-NE folding and shearing along C_2 planes. **e,f)** View from above, the subvertical S_1 foliation is affected by conjugate strike-slip vertical shear zones, indicating N-S pure-shear flattening. **g-i)** Interpreted field pictures of the two generations of folds. (h) & (i) are close-up views of the fold structure showing the orientations of P_1, P_2 and of the crenulation axial planes.

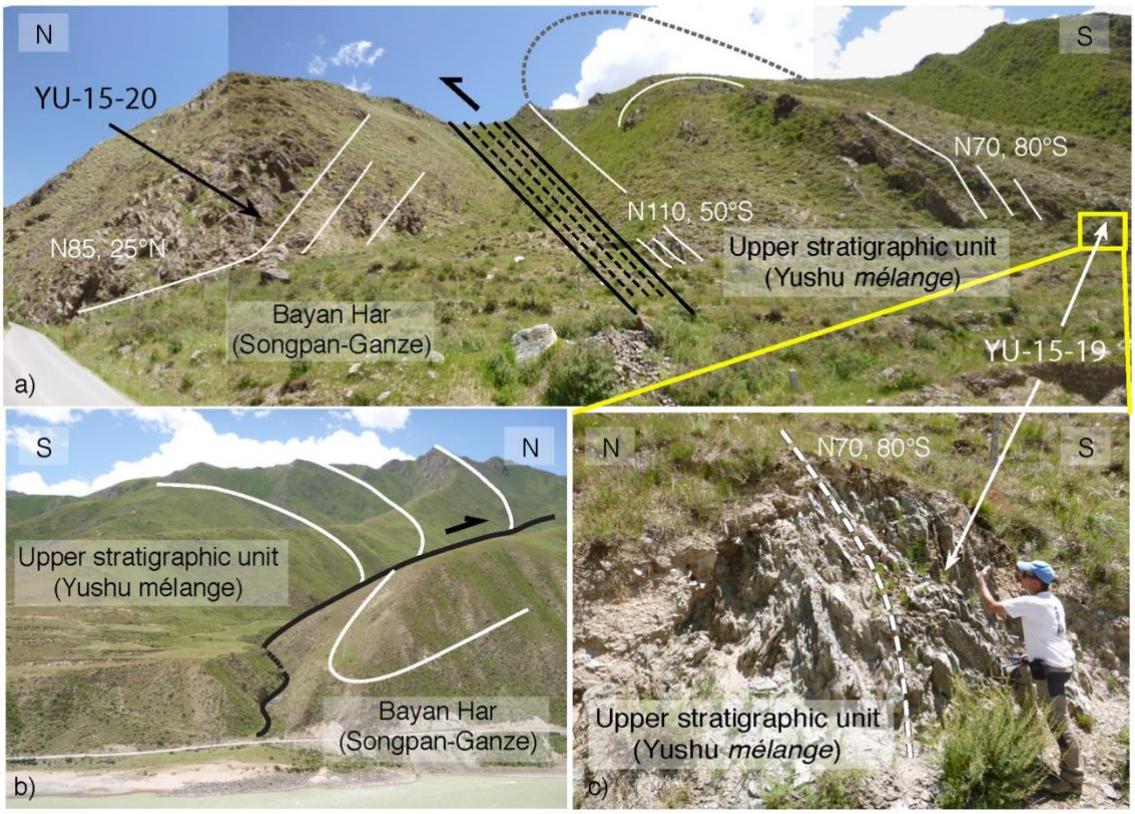

Figure 10. Top-to-the-north contact between the Yushu mélange upper stratigraphic unit and the Bayan Har turbidites of the Songpan-Ganze block, in the Zhiduo-Xiewu fault zone: **a, c)** outcrop views, with measured structural data reported (sampling site of YU-15-19 and YU-15-20); **b)** landscape view.

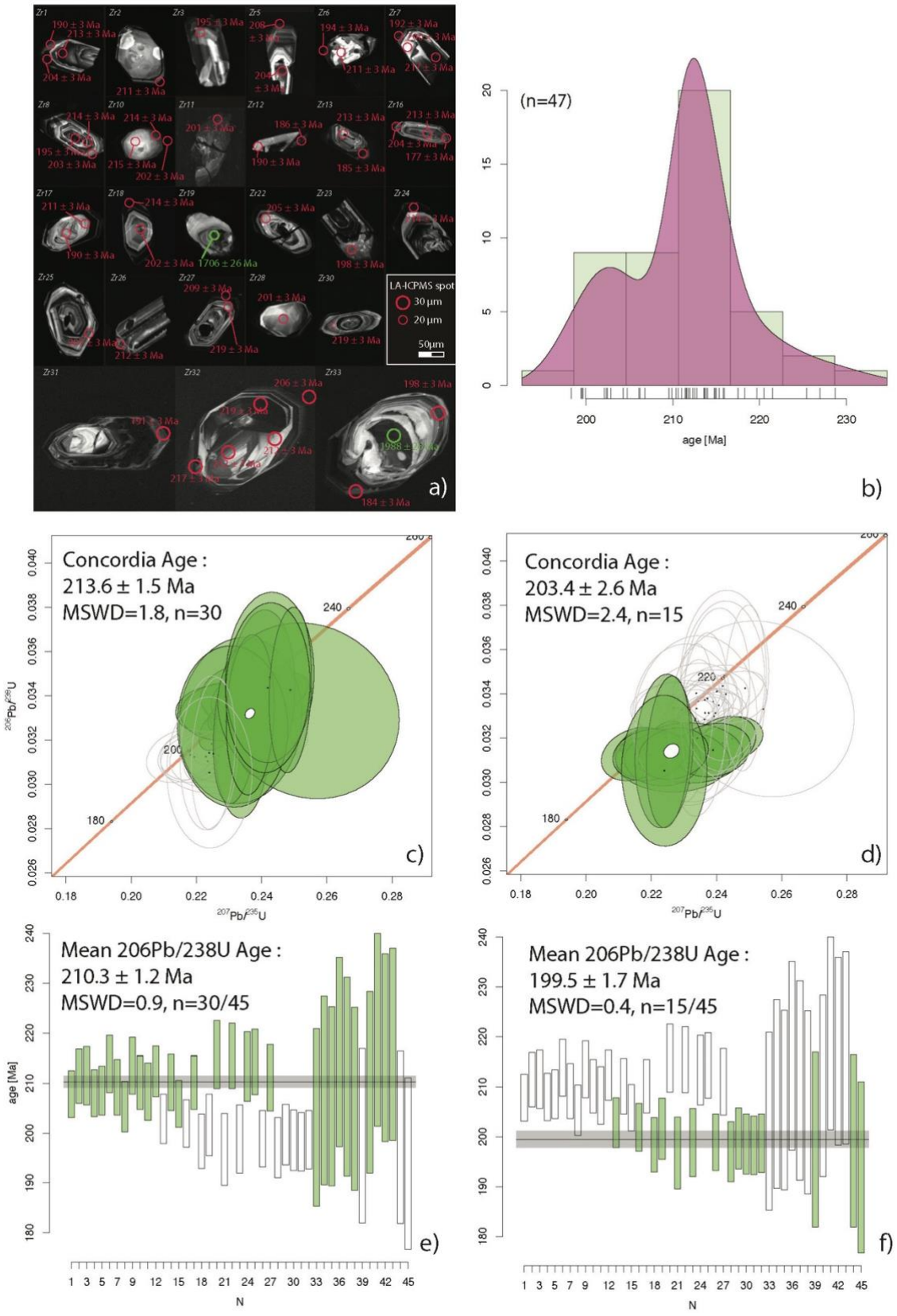

Figure 11. Zircon LA-ICP-MS U-Pb isotopic data and results for the mylonitic

granodiorite sample YU-14-63b. **a)** Zircons morphologies in CL microscopy, with laser-ablation spot locations. **b)** Zircon U-Pb age probability plots. **c,d)** Tera-Wasserburg concordia diagrams and **e,f)** mean $^{206}Pb/^{238}U$ age plots; the left panel (c,e) corresponds to the 30 oldest analyses, the right panel (d,f) to the 15 youngest.

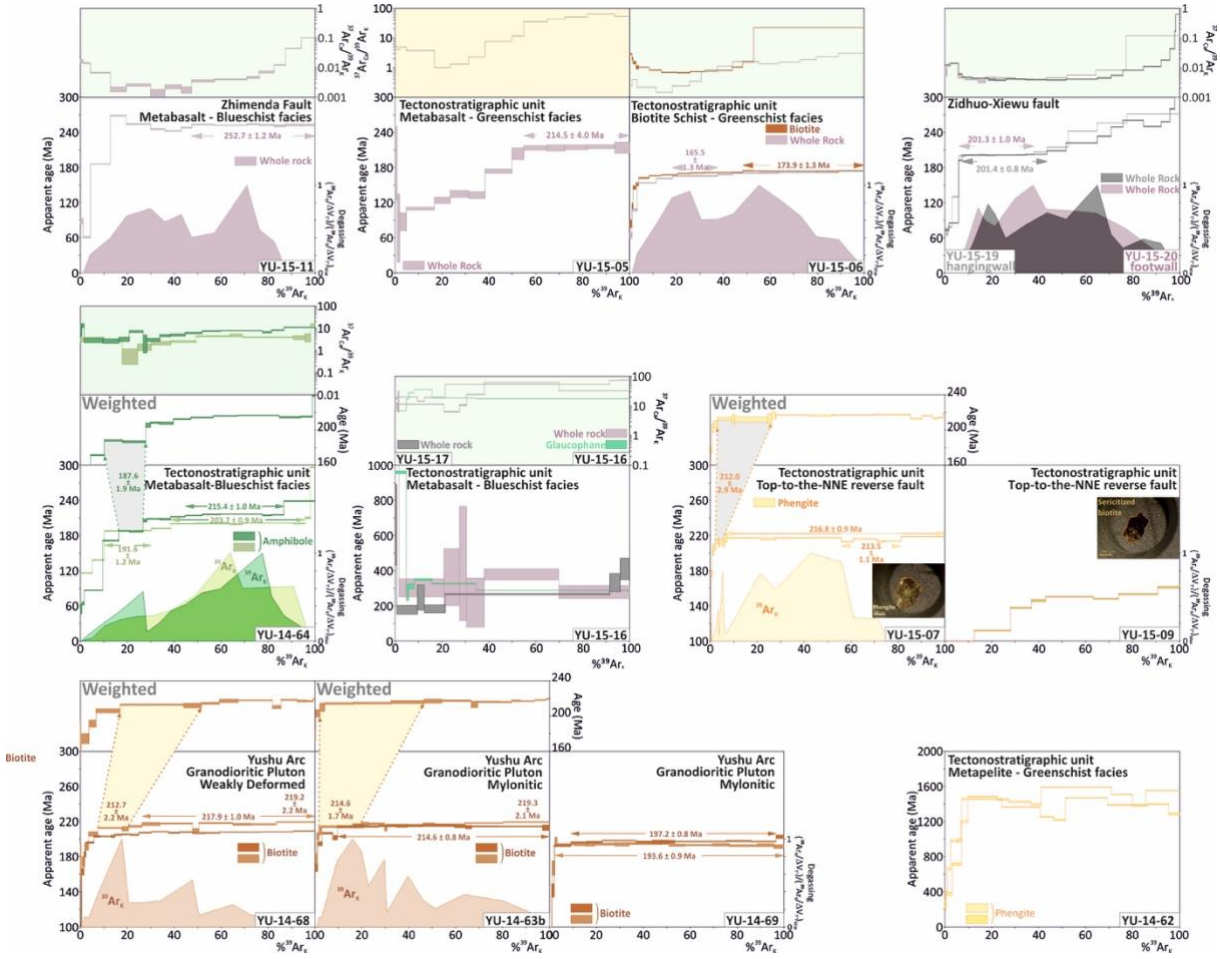

Figure 12. $^{40}Ar/^{39}Ar$ apparent age spectra of minerals and/or whole-rock fractions from deformed rocks from the Yushu mélange. Apparent age error bars are at the 1σ level; Errors in the J-parameter are not included. Plateau and pseudo-plateau ages (2σ uncertainties including errors in the J-parameter) are given when applicable. $^{39}Ar_K$ degassing spectra ($(^{39}Ar_K/DVT\circ)/(^{39}Ar_K/DVT\circ)Max$ vs. $\%^{39}Ar_K$) are provided for most of the experiments (See Tremblay et al. (2020) for a detailed explanation).

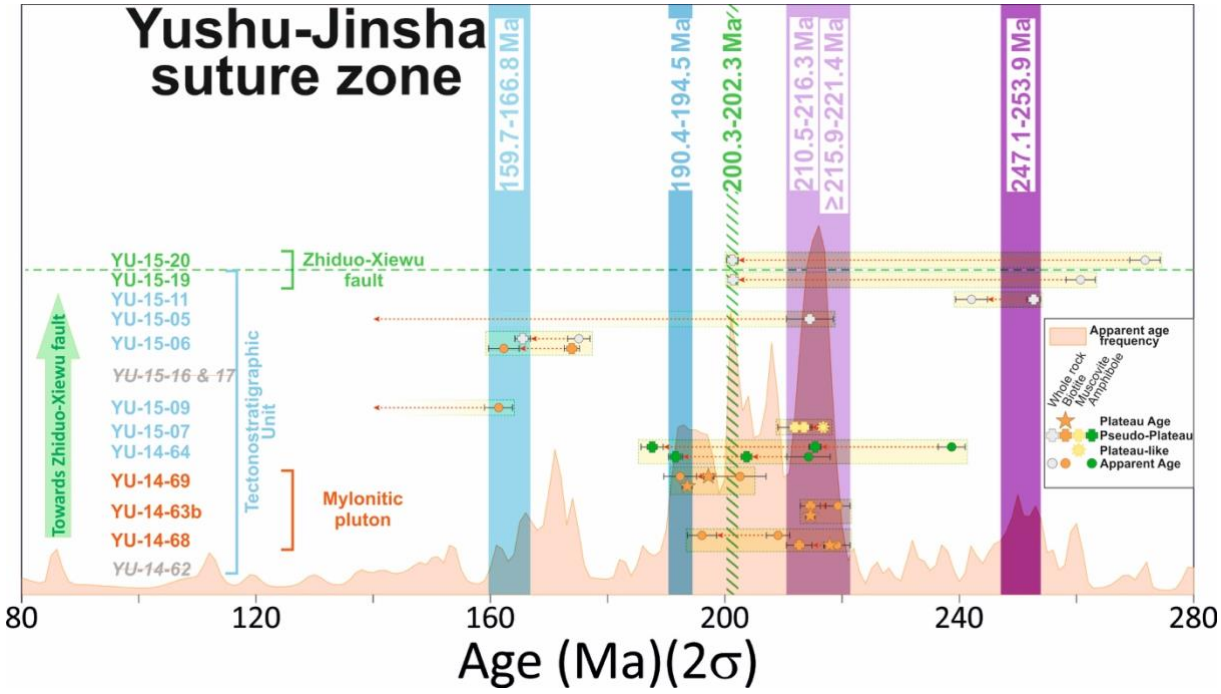

Figure 13. Synthesis of plateau, pseudo-plateau, plateau-like and apparent ages (2σ error bars) from $^{40}Ar/^{39}Ar$ analyses of whole rock (grey), biotite (brown), phengite (yellow) and amphibole (green) single grains from samples from the Tectonographic Unit and the Zhiduo-Xievu fault plotted against the frequency histogram (probability density diagrams) of the apparent ages (see Tremblay et al. (2020) for explanation). The samples are classified according to their sampling distance from the Zhiduo-Xiewu Fault. The main events identified by the $^{40}Ar/^{39}Ar$ geochronological study are highlighted by colour bars following the colour codes of the International Chronostratigraphic Chart. The significance of these periods is discussed in the text.

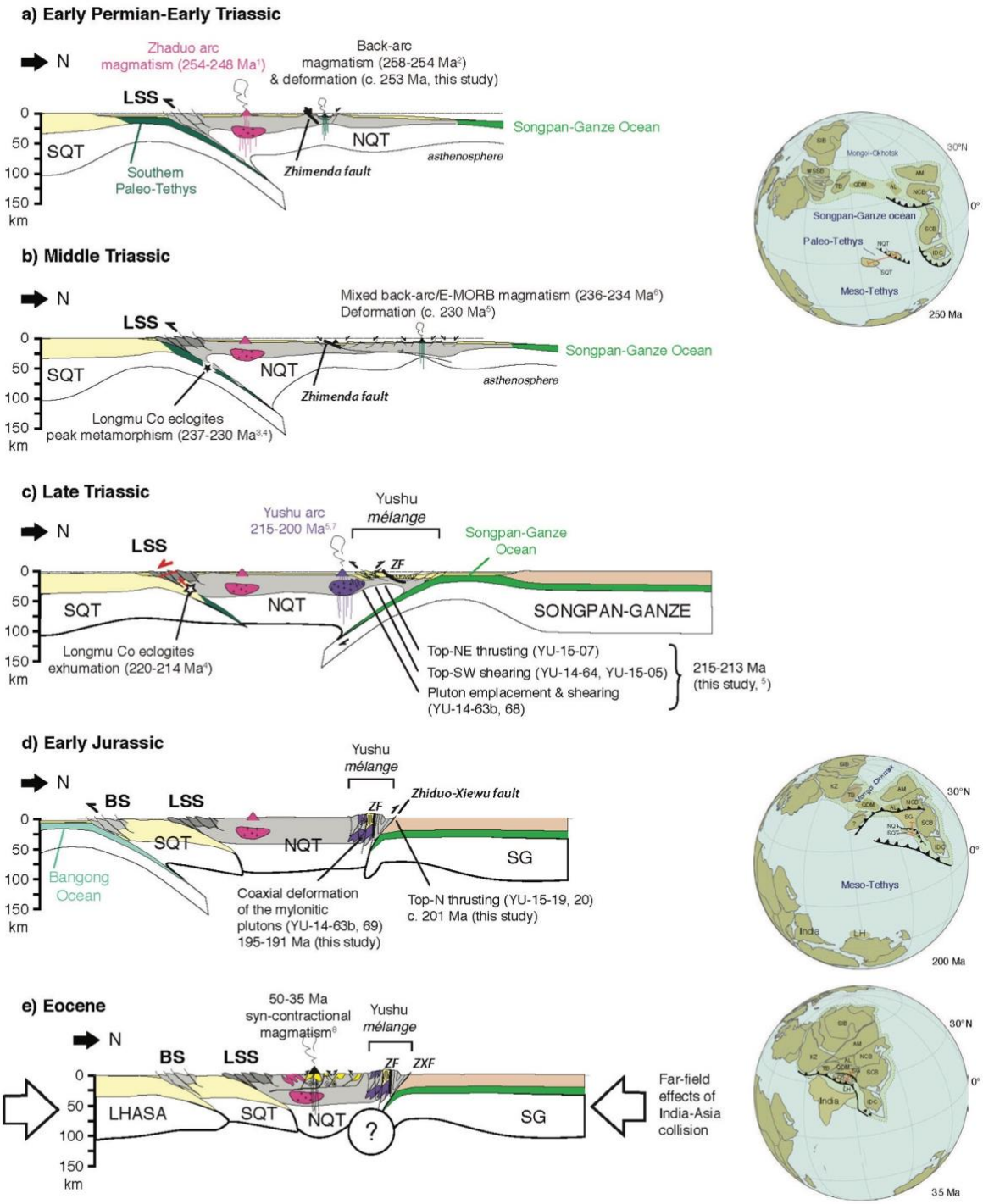

Figure 14. Schematic sketch (not to scale) of a possible geodynamic evolution of the Yushu area from the Permo-Triassic to the Eocene, reconciling the currently known ages of deformation and magmatism. Age data sources: [1]Yang et al. (2011); [2]Zhang et al. (2017); [3]Dan et al., 2018; [4]Zhai et al. (2011); [5]Yang et al. (2012); [6]Liu et al. (2016b); [7]Roger et al.

(2003); [8]Spurlin et al., 2005. Abbreviations: CQMB, Central Qiangtang Metamorphic Belt; BS, blueschist facies; JS, Jinsha-Ganze-Litang Suture; LSS, Longmu Co-Shuangu Suture; SQt, South Qiangtang; NQt, North Qiangtang.